# The clustering of H $\beta$ + [O III] and [O II] emitters since $z \sim 5$: dependencies with line luminosity and stellar mass

A. A. Khostovan,[1]★† D. Sobral,[2,3] B. Mobasher,[1] P. N. Best,[4] I. Smail,[5,6] J. Matthee,[3] B. Darvish,[7] H. Nayyeri,[8] S. Hemmati[9] and J. P. Stott[2,10]

[1]*Department of Physics & Astronomy, University of California, Riverside, USA*
[2]*Department of Physics, Lancaster University, Lancaster, LA1 4YB, UK*
[3]*Leiden Observatory, Leiden University, PO Box 9513, NL-2300 RA Leiden, the Netherlands*
[4]*SUPA, Institute for Astronomy, Royal Observatory of Edinburgh, Blackford Hill, Edinburgh EH9 3HJ, UK*
[5]*Centre for Extragalactic Astrophysics, Department of Physics, Durham University, Durham DH1 3LE, UK*
[6]*Institute for Computational Cosmology, Durham University, Durham DH1 3LE, UK*
[7]*Cahill Center for Astronomy and Astrophysics, California Institute of Technology, Pasadena, CA 91125, USA*
[8]*Department of Physics & Astronomy, University of California, Irvine, CA 92697, USA*
[9]*Infrared Processing and Analysis Center, California Institute of Technology, Pasadena, CA 91125, USA*
[10]*Sub-department of Astrophysics, Department of Physics, University of Oxford, Oxford OX1 3RH, UK*

## ABSTRACT

We investigate the clustering properties of $\sim$7000 H $\beta$ + [O III] and [O II] narrowband-selected emitters at $z \sim$ 0.8–4.7 from the High-$z$ Emission Line Survey. We find clustering lengths, $r_0$, of 1.5–4.0 $h^{-1}$ Mpc and minimum dark matter halo masses of $10^{10.7-12.1}$ M$_\odot$ for our $z = 0.8$–3.2 H $\beta$ + [O III] emitters and $r_0 \sim$ 2.0–8.3 $h^{-1}$ Mpc and halo masses of $10^{11.5-12.6}$ M$_\odot$ for our $z = 1.5$–4.7 [O II] emitters. We find $r_0$ to strongly increase both with increasing line luminosity and redshift. By taking into account the evolution of the characteristic line luminosity, $L^\star(z)$, and using our model predictions of halo mass given $r_0$, we find a strong, redshift-independent increasing trend between $L/L^\star(z)$ and minimum halo mass. The faintest H $\beta$ + [O III] emitters are found to reside in $10^{9.5}$ M$_\odot$ haloes and the brightest emitters in $10^{13.0}$ M$_\odot$ haloes. For [O II] emitters, the faintest emitters are found in $10^{10.5}$ M$_\odot$ haloes and the brightest emitters in $10^{12.6}$ M$_\odot$ haloes. A redshift-independent stellar mass dependency is also observed where the halo mass increases from $10^{11}$ to $10^{12.5}$ M$_\odot$ for stellar masses of $10^{8.5}$ to $10^{11.5}$ M$_\odot$, respectively. We investigate the interdependencies of these trends by repeating our analysis in a $L_{\rm line} - M_{\rm star}$ grid space for our most populated samples (H $\beta$ + [O III] $z = 0.84$ and [O II] $z = 1.47$) and find that the line luminosity dependency is stronger than the stellar mass dependency on halo mass. For $L > L^\star$ emitters at all epochs, we find a relatively flat trend with halo masses of $10^{12.5-13}$ M$_\odot$, which may be due to quenching mechanisms in massive haloes that is consistent with a transitional halo mass predicted by models.

**Key words:** galaxies: evolution – galaxies: haloes – galaxies: high-redshift – galaxies: star formation – cosmology: observations – large-scale structure of Universe.

## 1 INTRODUCTION

The current consensus of galaxy formation is that galaxies formed hierarchically inside dark matter haloes (see Benson 2010 for a review and references therein), suggesting that the two co-evolve. The question that arises then is how exactly are the physical properties of galaxies related to their host dark matter haloes? How significant

★ E-mail: akhostov@gmail.com
† NASA Earth and Space Science Fellow.

is this halo dependency on the evolution of a galaxy and at what cosmic times was this connection set in place?

Observationally, two-point correlation statistics trace the spatial clustering of galaxies and can provide us with insights of the underlying dark matter distribution. This then becomes helpful in relating the spatial clustering of galaxies as a function of their physical characteristics [e.g. star formation rate (SFR), mass, morphology] to dark matter halo properties to understand the galaxy–halo connection. It allows us to understand how the non-linear, stochastic

processes that affect baryons are connected to the simple, gravitational processes that govern dark matter halo growth.

With the advent of large galaxy photometric and spectroscopic surveys (e.g. SDSS: York et al. 2000, 2dFGRS: Colless et al. 2001, DEEP2: Davis et al. 2003, VVDS: Le Fèvre et al. 2005, PRIMUS: Coil et al. 2011, GAMA: Driver et al. 2011, BOSS: Dawson et al. 2013, VIPERS: Garilli et al. 2014, eBOSS: Dawson et al. 2016) in the last two decades, it has become possible to perform detailed analysis of clustering of galaxies as a function of their physical properties (e.g. colours, luminosities, SFRs, and stellar masses). At low redshifts ($z \sim$ 0–1), it has been found that red, passive galaxies are more clustered than blue, active galaxies (e.g. Norberg et al. 2002; Zehavi et al. 2005; Coil et al. 2008; Zehavi et al. 2011; Guo et al. 2013, 2014). Similar luminosity trends with clustering strength/halo mass are also observed at $z \sim$ 1–2 (e.g. Hartley et al. 2008; McCracken et al. 2010; Marulli et al. 2013; Ishikawa et al. 2015) and, using primarily Lyman Break galaxies (LBGs), at $z \sim$ 2–7 (e.g. Adelberger et al. 2005; Barone-Nugent et al. 2014; Harikane et al. 2016). Correlations between increasing stellar mass and increasing clustering strength/dark matter halo mass have also been reported in the literature (e.g. Meneux et al. 2008, 2009; Wake et al. 2011; Lin et al. 2012; Mostek et al. 2013; McCracken et al. 2015).

The significance of the results highlighted above suggests that dark matter haloes have an important role in the star formation processes that occur within galaxies. Large narrowband and spectroscopic surveys have been able to study how the clustering properties of galaxies correlate with star formation activity directly. Recent narrowband measurements using H $\alpha$ (tracing the instantaneous SFR) up to $z \sim$ 2 find that the clustering signal strongly increases with increasing H $\alpha$ line luminosity (Sobral et al. 2010; Stroe & Sobral 2015; Cochrane et al. 2017). Surprisingly, Sobral et al. (2010) found that the dependency is also redshift-independent in terms of $L/L^{\star}(z)$, with $L^{\star}(z)$ being the characteristic H $\alpha$ luminosity at each redshift, equivalent to a characteristic SFR (SFR$^{\star}$, Sobral et al. 2014). Other studies find similar line luminosity/SFR trends with clustering strength/halo mass up to $z \sim$ 2 (e.g. Mostek et al. 2013; Dolley et al. 2014; Coil et al. 2017). The trends observed by Sobral et al. (2010) also show a shallower/flat slope at $L > L^{\star}(z)$, which is suggested to be a signature of quenching processes within the most massive haloes.

Current results are primarily based on samples of the nearby Universe and a handful of $z \sim$ 1–2 studies. There are also a few LBG-selected samples up to $z \sim$ 7, but such samples are severely biased against dusty systems (e.g. Oteo et al. 2015), have photometric redshifts that are uncertain, and have complex selection functions. In order to effectively study the clustering properties of galaxies and understand how and when these galaxy–halo trends formed requires samples that (1) are well-defined in terms of selection criteria, (2) cover a range of redshifts to trace the evolving parameters over cosmic time, (3) cover multiple and large comoving volumes to reduce the effects of cosmic variance, (4) span a wide range in physical properties to properly subdivide the samples, and (5) have known redshifts.

In this study, we use a sample of H $\beta$ + [O III] and [O II] emission line-selected galaxies from Khostovan et al. (2015) to study the clustering properties and dependencies with line luminosity and stellar mass up to $z \sim$ 5 in four narrow redshift slices per emission line. Since our samples are emission line-selected, this gives us the advantage of knowing the redshifts of our sources within $\sigma_z = 0.01$–0.03 (based on the narrowband filter used) and forms a simple selection function, which is usually not the case with previous clustering studies using either broad-band filters or spectroscopic surveys. This also means that there is almost no redshift projection that can affect the measured clustering signals such that we can easily get high signal-to-noise clustering measurements using smaller samples in comparison to photometric and spectroscopic surveys, which typically span a very large redshift range and thus are subject to enormous projection effects. Lastly, our samples are also large enough ($\sim$7000 sources) to properly subdivide to study the dependency of galaxy properties on the clustering strength and spread over the COSMOS and UDS fields ($\sim$2 deg$^2$) to reduce the effects of cosmic variance.

This paper is structured as follows. In Section 2, we describe our emission line-selected samples used in the clustering measurements. In Section 3, we present our methodology of measuring the angular correlation function (ACF), discuss the effects of contamination, describe how we corrected for cosmic variance, present our measurements of the spatial correlation function, and describe our model to convert the clustering length to minimum dark matter halo mass. In Section 4, we analyse the results for the full sample measurements and then investigate the individual dependencies with halo mass starting with stellar mass and line luminosity. We then show the dependency with halo mass in a line luminosity–stellar mass grid space. In Section 5, we present our interpretations of the results. We present our main conclusions in Section 6.

Throughout this paper, we assume $\Lambda$ cold dark matter (CDM) cosmology with $H_0 = 70 \, \mathrm{km \, s^{-1}}$, $\Omega_m = 0.3$, and $\Omega_{\Lambda} = 0.7$. All stellar masses reported assume a Chabrier initial mass function.

## 2 SAMPLE

In this study, we use the large sample of H $\beta$ + [O III] and [O II] selected emission-line galaxies from the narrowband High-$z$ Emission Line Survey (HiZELS; Geach et al. 2008; Sobral et al. 2009, 2012, 2013) presented by Khostovan et al. (2015). Our samples are distributed over the COSMOS (Scoville et al. 2007) and UDS (Lawrence et al. 2007) fields with a combined areal coverage of $\sim$2 deg$^2$ that equates to comoving volume coverages of $\sim$10$^6$ Mpc$^3$. The sample consists of 3475 H $\beta$ + [O III] emitters at narrow redshift slices of $z = 0.84, 1.42, 2.23$, and 3.24 and 3298 [O II] emitters at $z = 1.47, 2.25, 3.34$, and 4.69. There are 223 and 219 spectroscopically confirmed H $\beta$ + [O III] and [O II] emitters, respectively, drawn from the UDSz Survey (Bradshaw et al. 2013; McLure et al. 2013), Subaru-FMOS measurements (Stott et al. 2013), Keck/DEIMOS and MOSFIRE measurements (Nayyeri et al., in preparation), PRISm MUlti-object Survey (PRIMUS; Coil et al. 2011), and VIMOS Public Extragalactic Redshift Survey (VIPERS; Garilli et al. 2014). Recent Keck/MOSFIRE measurements of $z = 1.47$–3.34 emitters are also included as well as recent VLT/VIMOS measurements for UDS sources (Khostovan et al., in preparation).

The selection criteria used are explained in detail in Khostovan et al. (2015). In brief, H $\beta$ + [O III] and [O II] emitters are selected based on a combination of spectroscopic measurements, photometric redshifts, and colour–colour selections (in order of priority) from the HiZELS narrowband colour excess catalogue of Sobral et al. (2013). Sources that have detections in multiple narrowband filters were also included in the final sample as the multiple emission line detections are equivalent to spectroscopic confirmation (e.g. the detection of [O II] in NB921 and H $\alpha$ in NBH, see Sobral et al. 2012; [O III] in NBH and H $\alpha$ in NBK, Suzuki et al. 2016; see also Matthee et al. 2016 and Sobral et al. 2017 for dual NB detections of Ly $\alpha$ and H $\alpha$ emitters at $z = 2.23$).

Stellar masses of the sample were measured by Khostovan et al. (2016) using the SED-fitting code of MAGPHYS (da Cunha, Charlot & Elbaz 2008), which works by balancing the stellar and dust components (e.g. the amount of attenuated stellar radiation is accounted for in the infrared). The level of active galactic nucleus (AGN) contamination was assessed by Khostovan et al. (2015) to be on the order of ∼10–20 per cent using the 1.6 μm bump as a proxy via the colour excesses in the *Spitzer* IRAC bands. Individual AGNs were not excluded from the sample due to the lack of X-ray detections (see Khostovan et al. 2015; Section 4.1). Overall, the sample covers a wide range in physical properties with stellar masses between $10^{8-11.5}$ M$_\odot$, EW$_{rest}$ between 10 and 10 000 Å, and line luminosities between $10^{40.5-43.0}$ erg s$^{-1}$, providing a wealth of different types of 'active' galaxies (star-forming + AGN; Khostovan et al. 2016). This is important when investigating the connection between physical and clustering properties of galaxies.

A unique advantage of narrowband surveys in terms of clustering studies is knowing the redshift distribution of each line (emission line-selected), which removes any redshift projections. Fig. 1 shows the spatial distribution of the NBJ samples (H β + [O III] $z = 1.42$ and [O II] $z \sim 2.25$) where, visually, it is clear that sources in both samples have a non-random, spatial clustering.

## 3 METHODOLOGY

### 3.1 Generating the random sample

When looking for a clustering signal, an equivalent and consistent random catalogue is required to test for a non-random spatial distribution within the sample. If all the sources within the sample are consistent with a random spatial distribution, then no spatial correlation would exist within the errors. Therefore, the methodology of creating the random sample has to be consistent with the real data set in terms of depth, survey geometry, and masked regions (see Fig. 1).

We create our random samples on an image-by-image basis in order to take into account the different survey depths.[1] As we also want to investigate the dependency with line luminosity and stellar mass (see Sections 4.2–4.4), we populate each image using the line luminosity functions of Khostovan et al. (2015). For each image, we calculate the total effective area that takes into account the masked areas. We then integrate the Khostovan et al. (2015) luminosity functions down to the $3\sigma$ detection limit of each image to calculate the total number of sources expected within the image area. This is then rescaled up by a factor of $10^5$ such that each random sample generated has a total of ∼$10^6$ mock sources for each field. Fig. 1 shows the masked regions of the NBJ images for both the COSMOS and UDS fields that are taken into account when generating the random samples.

### 3.2 Angular correlation function

We use the Landy & Szalay (1993, LS) estimator to measure the two-point ACF defined as

$$w(\theta) = 1 + \left(\frac{N_R}{N_D}\right)^2 \frac{DD(\theta)}{RR(\theta)} - 2\frac{N_R}{N_D}\frac{DR(\theta)}{RR(\theta)}, \tag{1}$$

[1]Refer to table 2 of Sobral et al. (2013) for information regarding the depth of each image.

where $w(\theta)$ is the ACF, DD is the number of data–data pairs, RR is the number of random–random pairs, DR is the number of data–random pairs, $\theta$ is the angular separation, and $N_R$ and $N_D$ are the total number of random and data sources, respectively. The error associated with the LS estimator is defined as

$$\Delta w(\theta) = \frac{1 + w(\theta)}{\sqrt{DD(\theta)}}, \tag{2}$$

which assumes Poisson error. We refer the reader to Landy & Szalay (1993) for technical details about the estimator and Kerscher, Szapudi & Szalay (2000) for a comparison with other known two-point correlation estimators.

Due to our small sample sizes in comparison to other clustering studies, binning effects could introduce uncertainties in measuring the ACFs. This is a signal-to-noise problem where if the bins are too small, then the measured data–data pairs (signal) are not sufficiently populated such that the random–random pairs (noise) dominates the measured ACF.

To take this into account, we adopt the approach of Sobral et al. (2010) and measure the ACF 2000 times assuming Poisson errors as described in equation (2) with varying bin centres and sizes. For each ACF, we apply a random bin size ($\Delta\log\theta = 0.05$–$0.25$ dex) with $\theta_{min} = 1.0$–$5.0$ arcsec (randomly selected per ACF) and $\theta_{max} = 3100$ arcsec. Each realization draws 10–100 times the number of real sources from the random sample discussed in Section 3.1 and the number of data–data, random–random, and data–random pairs are measured. We then fit a power law of the form

$$w(\theta) = A_w(\theta^\beta - IC)$$
$$IC = \frac{\sum RR\theta^\beta}{\sum RR}, \tag{3}$$

with $A_w$ as the clustering amplitude and $\beta$ as the power-law slope fixed at $-0.8$. The second equation is the integral constraint (IC; Roche et al. 2002) that takes into account the limited survey area. We note that the IC has a marginal effect on our measurements of $r_0$ as HiZELS coverage is $>1$ deg$^2$. The final measurements and errors for $A_w$ and the clustering length ($r_0$; see Section 3.4) are based on the distributions of values from the 2000 ACFs. In this way, we take into account the effects associated with binning. We find that our approach of assuming Poisson errors is consistent with measuring errors via bootstrapping assuming a fixed bin size and centre and refer the reader to Appendix C for details. The final ACFs are shown in Fig. 2 and discussed in Section 4.1.

Our measurements are corrected for cosmic (sample) variance by using the empirical relation measured by Sobral et al. (2010), where the uncertainty in $A_w$ (in percentage) is related to the survey area as $20 \times \Omega^{-0.35}$, with $\Omega$ representing the area in units of deg$^2$. Our survey size of ∼2 deg$^2$ corresponds to an uncertainty of ∼16 per cent due to cosmic variance in the measurement of $A_w$. We incorporate this uncertainty by adding ∼16 per cent of $A_w$ in quadrature to the error from the fit. For the clustering length, $r_0$, we propagate the error from $A_w$ and find that the error in $r_0$ is increased by ∼11 per cent.

### 3.3 Effects of contamination

The issue of contamination within the sample can be marginal or quite significant and is based on many factors such as the sample selection. Clustering studies typically consider the contaminants in a sample to be randomly distributed, such that the clustering amplitude is underestimated by a factor of $(1 - f)^2$, with $f$ being the
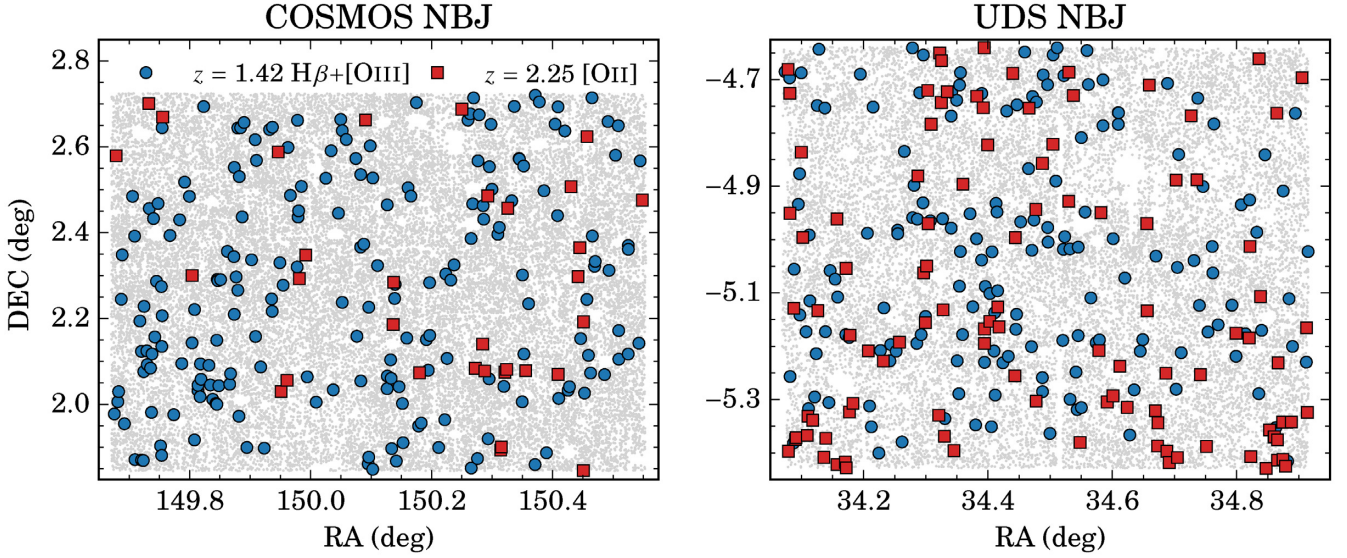
## COSMOS NBJ

## UDS NBJ



**Figure 1.** The full COSMOS and UDS on-sky coverages with the NBJ filter. Shown in *blue circles* and *red squares* are the $z = 1.42$ H $\beta$ + [O III] and $z = 2.25$ [O II] emitters, respectively. The *grey dots* are all sources in the raw catalogue used to select emission-line galaxies and clearly outline the masked regions that are associated with bright stars and artefacts. We refer the reader to Sobral et al. (2013) for a detailed description of how the masked regions were identified. The spatial distributions show, visually and qualitatively, signatures of a non-random distribution. To properly quantify the clustering signal, we need to produce random samples that carefully take into account masked regions as outlined above.
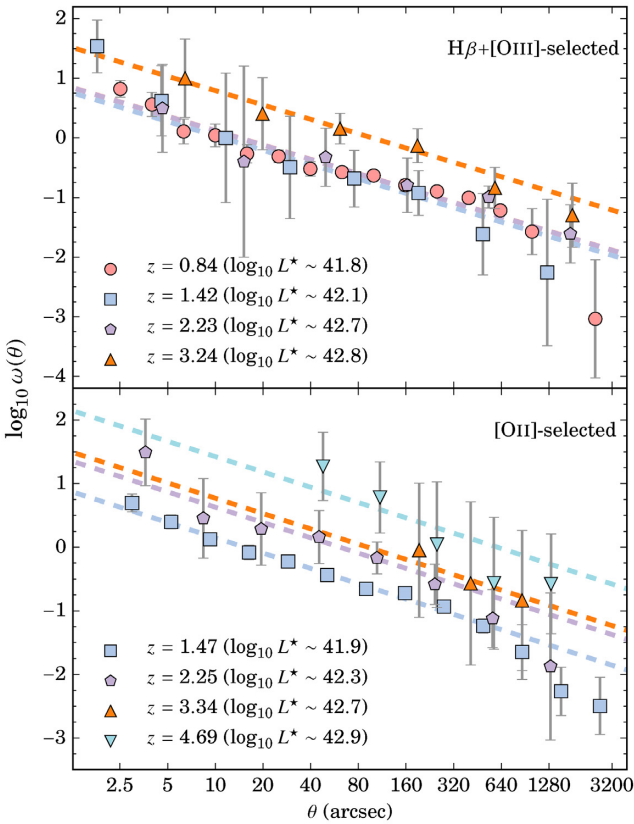


**Figure 2.** The angular correlation function based on the median of all the 2000 realizations per sample with the corresponding Limber approximation fits. All ACFs are calculated using the LS estimator. The fits shown are constrained to angular separations for which the ACF is best described by a power law with slope, $\beta = -0.8$. There is evidence for an evolution in the clustering amplitude, but we stress the point that the clustering signal is sensitive to the range of physical properties (e.g. luminosity and stellar mass), which we explore in Section 4.

contamination fraction. For the clustering length, $r_0$, this results in an underestimation by a factor of $(1 - f)^{2/|\gamma|}$.

The level of contamination was briefly investigated in Khostovan et al. (2015) and was found to be on the order of $\sim 10$ per cent for the lowest redshift samples. This would result in a 23 per cent increase in $A_w$ and a 12 per cent increase in $r_0$. Note that this assumes that the contaminants are randomly distributed and, hence, lower the clustering strength, which may not be true for narrowband surveys. For our samples, contaminants could be due to galaxies with misidentified emission lines. For example, a source at $z = 1.47$ that is misidentified as [O II] in the NB921 filter could actually be a $z = 0.84$ [O III] emitter or a $z = 0.40$ H $\alpha$ emitter. Because galaxies selected by nebular emission lines are shown to be clustered as well (see below and Sobral et al. 2010 and Cochrane et al. 2017 for H $\alpha$), the effects could be negligible and not follow the typical $(1 - f)^2$ correction factor. Therefore, we do not correct our measurements due to contamination.

### 3.4 Spatial correlation function

The two-point (spatial) correlation function is a useful tool in measuring the physical clustering of galaxies and is best described, empirically, by $\xi = (r/r_0)^\gamma$, with $r_0$ being the clustering length. Typically, the Limber approximation (Limber 1953) is used to relate the spatial and angular correlation functions, but Simon (2007) found that this approximation breaks down at larger angular separations and when redshift distributions become more like a delta function. In such cases, they find that the observed angular correlation function becomes a rescaled version of $\xi(r)$ with the slope of $w(\theta)$ changing from $\gamma + 1$ to $\gamma$. This has been observed by various narrowband studies (e.g. Guaita et al. 2010; Sobral et al. 2010; Geach et al. 2012; Stroe & Sobral 2015; Bielby et al. 2016; Cochrane et al. 2017; Ouchi et al. 2018).

We adopt the exact equation presented by Simon (2007) and used by Sobral et al. (2010) to relate the real-space and angular

**Table 1.** Properties of the narrowband filters and their Gaussian representations.

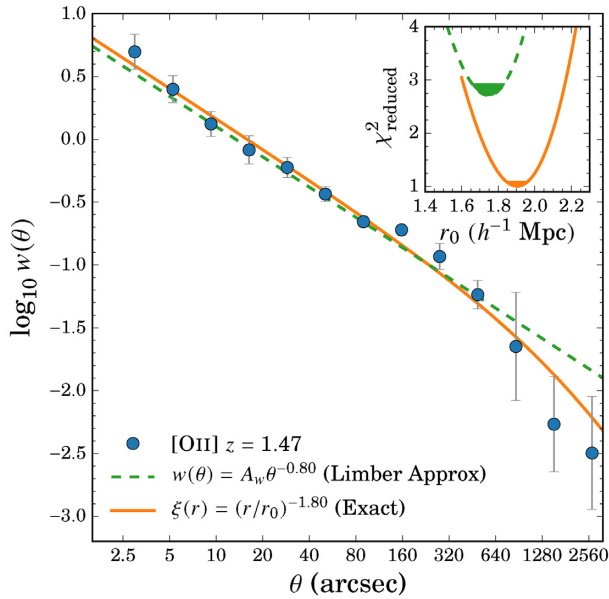| Filter | Narrowband filter | | | Gaussian filter | | |
|---|---|---|---|---|---|---|
| | $\lambda_{obs}$ (Å) | FWHM (Å) | $r_{c,H\beta+[O\,III]}$ (Mpc $h^{-1}$) | $\sigma_{H\beta+[O\,III]}$ (Mpc $h^{-1}$) | $r_{c,[O\,II]}$ (Mpc $h^{-1}$) | $\sigma_{[O\,II]}$ (Mpc $h^{-1}$) |
| NB921 | 9196 | 132 | 2016 | 20 | 3008 | 19 |
| NBJ | 12110 | 150 | 2945 | 16 | 3862 | 14 |
| NBH | 16170 | 211 | 3846 | 15 | 4663 | 14 |
| NBK | 21210 | 210 | 4601 | 10 | 5323 | 9 |



**Figure 3.** The angular correlation function for the $z = 1.47$ [O II] sample. Shown are the observed $w(\theta)$ measurements as in Fig. 2 with the corresponding Limber approximation and exact equation fits. We use the full range of angular separations for both fits, even though the Limber approximation fails at $\theta \sim 500$ arcsec. The exact equation results in a reduced $\chi^2 \approx 1$ and $r_{0,\,exact} = 1.90 \pm 0.21$, while the Limber approximation results in a reduced $\chi^2 \approx 2.8$ and $r_{0,\,exact} = 1.75 \pm 0.21$. Errors shown in the $\chi^2$ distribution are only based on the fits. The results shown here signify the importance of the exact Limber equation when using narrowband samples for large angular separations.

correlation functions and calculate $r_0$. The relation is described as

$$\omega(\theta) = \frac{r_0^{-\gamma}}{1 + \cos\theta} \int\limits_{0}^{\infty} \int\limits_{\bar{r}\sqrt{2(1-\cos\theta)}}^{2\bar{r}} \frac{2p(\bar{r}-\Delta)p(\bar{r}+\Delta)}{R^{-\gamma-1}\Delta} \mathrm{d}R\mathrm{d}\bar{r}$$

$$\Delta = \sqrt{\frac{R^2 - 2\bar{r}^2(1-\cos\theta)}{2(1+\cos\theta)}}, \tag{4}$$

where $p$ is the filter profile in radial comoving distance units, $\bar{r} = (r_1 + r_2)/2$ as the mean spatial position of two sources, $R$ as the distance between the two sources, and $\gamma = -1.8$ ($\gamma = \beta - 1$) as the power-law slope of the spatial correlation function. Filter profiles are best represented as single Gaussians and trace the redshift distribution of the sample. The parameters of the filters and Gaussian representations are described in Table 1. We use equation (4) to fit $r_0$ to our measurements of $w(\theta)$.

Fig. 3 shows the comparison between the Limber approximation [assuming a single power law to describe $w(\theta)$ as shown in equa-

tion (3)] and the exact Limber equation as described in equation (4) for the $z = 1.47$ [O II] sample. We find that the Limber approximation breaks down at angular separations of $\gtrsim 500$ arcsec. Using the Limber approximation results in $r_{0,\,limber} = 1.75 \pm 0.21$ $h^{-1}$ Mpc and reduced $\chi^2 = 2.8$, while using the approach of Simon (2007) results in $r_{0,\,exact} = 1.90 \pm 0.21$ $h^{-1}$ Mpc and reduced $\chi^2 \sim 1$. Although both methods produce measurements that are consistent within $1\sigma$ (errors dominated by cosmic variance), our results shown in Fig. 3 highlight the importance of using the exact Limber equation to measure the clustering length since it can compensate for the rescaling of the ACF and provides a better reduced $\chi^2$. Throughout the rest of this paper, we refer to $r_0$ as the clustering length measured using equation (4).

### 3.5 Dark matter halo model

Our theoretical understanding of galaxy formation is that galaxies form with the assistance of the gravitational potentials of their host dark matter haloes. In effect, the spatial clustering of galaxies is then related to the clustering of dark matter. Matarrese et al. (1997) and Moscardini et al. (1998) used this link between galaxies and dark matter haloes to predict the clustering length of a sample for a given minimum dark matter halo mass and redshift. In this section, we use the same methodology used to generate their predictions, but update to the latest cosmological prescriptions.

We first begin by measuring the matter–matter spatial correlation function using a suite of cosmological codes named `colossus` (Diemer & Kravtsov 2015). This is calculated by taking the Fourier transform of the matter power spectrum, assuming an Eisenstein & Hu (1998) transfer function. We then calculate the effective bias by using the following equation:

$$b_{eff}(z) = \frac{\int_{M_{min}}^{\infty} b_h(M, z)\langle N_g(M, z)\rangle n(M, z)\mathrm{d}M}{\int_{M_{min}}^{\infty} \langle N_g(M, z)\rangle n(M, z)\mathrm{d}M}, \tag{5}$$

where $b_h(M, z)$ and $n(M, z)$ are the halo bias and mass functions, respectively, $\langle N_g(M, z)\rangle$ is the average galaxy–halo occupation, and $M_{min}$ is the minimum dark matter halo mass. The effective bias is related to the spatial correlation of galaxies by

$$b_{eff}^2 = \xi_{gg}/\xi_{mm}, \tag{6}$$

with $\xi_{gg}$ and $\xi_{mm}$ being the galaxy–galaxy and matter–matter spatial correlation functions, respectively.

We use the Tinker et al. (2010) halo bias prescription and the Tinker et al. (2008) halo mass function. The previous predictions of Matarrese et al. (1997) and Moscardini et al. (1998) used the Press & Schechter (1974) halo mass function and Mo & White (1996) halo bias functions. Their assumed $\Lambda$CDM cosmology was also different ($H_0 = 65$ km s$^{-1}$ Mpc$^{-1}$, $\Omega_m = 0.4$, and $\Omega_\Lambda = 0.6$) than the current measurements. We present a discussion regarding the uncertainties of assuming a bias and mass function in Appendix A.

**Table 2.** The clustering properties for our H $\beta$ + [O III] and [O II] samples. The power-law slope, $\beta$, in the ACF is shown and corresponds to the clustering amplitude, $A_{w,\,\text{free}}$, which corresponds to when $\beta$ is a free parameter in the fit. All other measurements shown have $\beta$ fixed to $-0.8$, which corresponds to $\gamma = -1.8$ in the real-space two-point correlation function. $r_{0,\,\text{exact}}$ is the clustering length measured using the exact Limber equation as defined in equation (4). Dark matter halo masses are measured using our $r_0$-halo mass models. The reduced chi-sq, $\chi^2_{\text{red}}$, is based on the exact equation fits using the Levenberg–Marquardt algorithm.

| | | | | | | | |
|---|---|---|---|---|---|---|---|
| | | | **Clustering properties for full sample** | | | | |
| $z$ | $N_{\text{D}}$ | $\beta$ | $A_{w,\,\text{free}}$ (arcsec) | $A_{w,\,\beta=-0.8}$ (arcsec) | $r_{0,\,\text{exact}}$ (Mpc $h^{-1}$) | $\log_{10} M_{\text{min}}$ (M$_\odot$ $h^{-1}$) | $\chi^2_{\text{red}}$ |
| | | | H $\beta$ + [O III] Emitters | | | | |
| 0.84 | 2477 | $-0.69^{+0.03}_{-0.03}$ | $5.19^{+1.32}_{-1.22}$ | $11.53^{+2.33}_{-2.33}$ | $1.71^{+0.19}_{-0.19}$ | $11.18^{+0.33}_{-0.33}$ | 3.01 |
| 1.42 | 371 | $-0.79^{+0.07}_{-0.04}$ | $7.47^{+3.58}_{-3.24}$ | $8.32^{+2.18}_{-2.08}$ | $1.45^{+0.20}_{-0.20}$ | $10.70^{+0.40}_{-0.40}$ | 0.18 |
| 2.23 | 270 | $-0.81^{+0.15}_{-0.12}$ | $11.10^{+12.42}_{-6.57}$ | $10.42^{+2.80}_{-2.62}$ | $2.43^{+0.31}_{-0.31}$ | $11.61^{+0.22}_{-0.22}$ | 0.37 |
| 3.24 | 179 | $-0.78^{+0.04}_{-0.03}$ | $42.28^{+13.22}_{-13.56}$ | $48.70^{+10.71}_{-10.83}$ | $4.01^{+0.49}_{-0.49}$ | $12.08^{+0.17}_{-0.17}$ | 0.12 |
| | | | [O II] Emitters | | | | |
| 1.47 | 3285 | $-0.83^{+0.02}_{-0.04}$ | $10.06^{+2.66}_{-2.21}$ | $11.61^{+2.34}_{-2.34}$ | $1.99^{+0.22}_{-0.22}$ | $11.46^{+0.23}_{-0.24}$ | 1.01 |
| 2.25 | 137 | $-0.78^{+0.05}_{-0.03}$ | $25.51^{+9.08}_{-9.18}$ | $29.99^{+7.24}_{-7.00}$ | $3.14^{+0.43}_{-0.41}$ | $12.03^{+0.21}_{-0.20}$ | 0.16 |
| 3.34 | 35 | $-0.79^{+0.23}_{-0.06}$ | $53.67^{+41.66}_{-44.95}$ | $57.49^{+22.49}_{-24.67}$ | $5.06^{+1.08}_{-0.94}$ | $12.37^{+0.28}_{-0.24}$ | 0.13 |
| 4.69 | 18 | $-0.83^{+0.04}_{-0.04}$ | $208.50^{+116.82}_{-91.58}$ | $139.44^{+53.69}_{-44.63}$ | $8.25^{+1.54}_{-1.44}$ | $12.62^{+0.22}_{-0.20}$ | 0.26 |

For the galaxy–halo occupation, we consider the simple case of $\langle N_g(M, z) \rangle = 1$ where every dark matter halo is occupied by a single central galaxy. Typical halo occupation distribution (HOD) models consider satellite galaxy contributions, a wide range of parameter space, and detailed prescriptions for galaxy–halo occupation (e.g. Kravtsov et al. 2004; Zheng et al. 2005). For narrowband studies, such as this one, the survey depths are too shallow to capture faint, satellite galaxies. For example, Geach et al. (2012) and Cochrane et al. (2017) used the H $\alpha$ HiZELS samples between $z \sim 0.8$–2.2 and found a negligible satellite fraction of $\sim 5$ per cent. We can safely then assume that our samples are made up of primarily central galaxies (see Section 4.1).

We also note that our samples are flux-complete down to a limiting flux, but are not stellar mass-complete. Although this could potentially cause problems in terms of how we are assigning galaxies to haloes, we show further in this study that halo masses are consistent with abundance matching studies when looking at the stellar–halo mass (SHM) relationship (see Section 4.2). We also show a comparison between our $r_0$-DMH model measurements and those drawn from the literature in Appendix B and find that our minimum halo masses measured from our model are consistent with the effective halo masses from typical HOD models.

## 4 RESULTS

### 4.1 Clustering properties of H $\beta$ + [O III] and [O II] emitters

The angular and spatial distributions of galaxies encode information regarding their clustering properties and, in turn, the types of dark matter haloes for which they reside in. Our measured angular correlation functions for our samples are shown in Fig. 2 with the respective best-fitting model overlaid. As shown in Table 2, we fit the observed ACFs using equation (3) with $\beta$ as a free parameter and find that our measurements are within $\sim 1\sigma$ of the fiducial slope of $-0.8$. We therefore fix $\beta = -0.8$ throughout the rest of this paper.

Fig. 2 shows the median $w(\theta)$ for all 2000 realizations with the best-fitting $A_w$ defining the power law. There are weak signs of the 1-halo term (small-scale clustering/contribution of satellite galaxies) at angular separations <20 arcsec ($\sim 150$ kpc) for the $z = 0.84$

H $\beta$ + [O III] sample and the deviation from the power-law fit (although within $1\sigma$) is consistent with the 1-halo term. We find no significant detection of the 1-halo term in the [O II] samples. This implies that the fraction of satellite galaxies within our samples is quite low, which is consistent with other emission line galaxy studies (e.g. Geach et al. 2012; Cochrane et al. 2017; H $\alpha$ satellite fractions of $\sim 5$ per cent). One possible reason for the presence of the 1-halo term for the $z = 0.84$ H $\beta$ + [O III] ACF could be due to the $\sim 10$ Mpc-scale overdense region in the COSMOS field, which contains several X-ray-confirmed clusters/groups and large filaments (e.g. Sobral et al. 2011; Darvish et al. 2014), but we defer from a detailed analysis of the satellite fractions as it is beyond the scope of this work. Overall, our samples are dominated by central galaxies that allows us to ignore the effects of a satellite population of galaxies in our dark matter halo model (see Section 3.5).

We explore the spatial correlation of our samples using our observed measurements of the angular correlation functions as described in equation (4) and in Section 3.4. The spatial correlation allows us to investigate the clustering of galaxies in terms of the physical projection between two galaxies and is characterized by the clustering length ($r_0$). Fig. 4 shows the evolution of $r_0$ for H $\beta$ + [O III] and [O II] emitters up to $z \sim 3$ and $\sim 5$, respectively. Included are the $r_0$ predictions for dark matter haloes with minimum masses between $10^{11}$ and $10^{13}$ M$_\odot$ based on our model described in Section 3.5.

We find that H $\beta$ + [O III] emitters tend to reside in $\sim 10^{10.7}$–$10^{12.1}$ M$_\odot$ dark matter haloes, while the [O II] emitters are found to vary less with $\sim 10^{11.5}$ M$_\odot$ at $z = 1.47$ to $\sim 10^{12.6}$ M$_\odot$ at $z = 4.69$, although these are primarily driven by selection effects. In comparison to each other, all overlapping samples, except for the $z \sim 1.5$ samples, have similar $r_0$ measurements within $1\sigma$ error bars. This then suggests that H $\beta$ + [O III]- and [O II]-selected galaxies reside in dark matter haloes with similar masses.

Included in Fig. 4 are the H $\alpha$ measurements of Shioya et al. (2008), Sobral et al. (2010), Stroe & Sobral (2015), Cochrane et al. (2017), and Kashino et al. (2017). The Sobral et al. (2010) measurement at $z = 2.23$ is consistent with that of the H $\beta$ + [O III] and [O II] samples at the same redshift, suggesting that
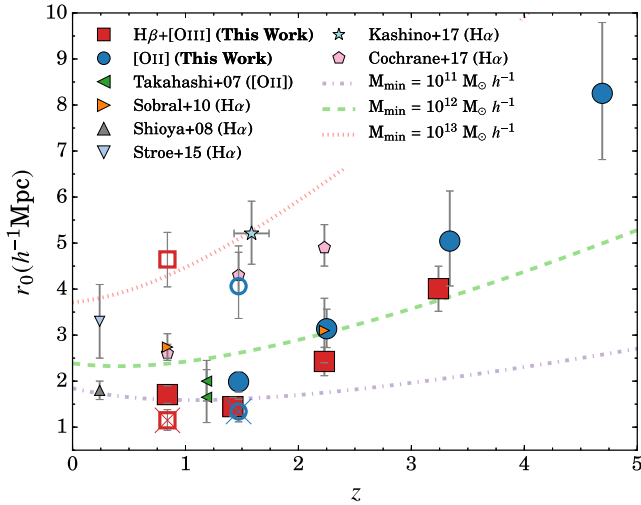
**Figure 4.** Shown is the evolution of the clustering length up to $z \sim 5$. Included are the predicted clustering lengths for minimum dark matter halo masses between $10^{11-13}$ M$_\odot$. Although there is a clear sign of a redshift evolution in $r_0$, we stress the point that this is due to selection bias such that these measurements are sensitive to the range of physical properties, such as line luminosity. As a demonstration, we overlay the brightest (*open symbol*) and faintest (*open symbol with a cross*) line luminosity bins (see Table 3) with the symbol type and colour consistent with that used for the full sample measurement. The brightest emitters are found to have $r_0$ measurements ∼2–3 times that of the full sample and the faintest emitters with ∼50 per cent lower $r_0$ values.

H $\beta$ + [O III]- and [O II]-selected emitters reside in dark matter haloes with similar masses as H $\alpha$-selected emitters and can be tracing a similar underlying population of star-forming/active galaxies. We also include the $z \sim 1.2$ [O II] measurements of Takahashi et al. (2007). Although our closest sample in terms of redshift is at $z = 1.47$, we find that our measurements are in agreement.

Despite the agreement between H $\alpha$, H $\beta$ + [O III], and [O II] samples, we note that such a comparison is not entirely fair. A comparison between the H $\alpha$ measurements of Stroe & Sobral (2015, 26 deg$^2$ survey, $3\sigma$ $F_{lim} \sim 7.3 \times 10^{-16}$ ergs s$^{-1}$ cm$^{-2}$) and those of Shioya et al. (2008, 1.5 deg$^2$ survey, $3\sigma$ $F_{lim} \sim 7 \times 10^{-18}$ ergs s$^{-1}$ cm$^{-2}$) shows a difference of a factor of 2 in $r_0$ and a difference of two orders of magnitude in minimum dark matter halo mass. This is due to sample bias as a result of the survey parameters where the Stroe & Sobral (2015) sample is dominated by the brightest emitters relative to the Shioya et al. (2008) sample.

As a demonstration of this same feature, we show $r_0$ of the brightest (open symbols) and faintest (open symbols with a cross) galaxies in our H $\beta$ + [O III] $z = 0.84$ and [O II] $z = 1.47$ samples in Fig. 4. We find that the most luminous (faintest) galaxies have higher (lower) clustering lengths relative to the full sample measurement. It is then not surprising that we find higher $r_0$ with increasing redshift as a result of Malmquist bias. This leads to the conclusion that any comparison needs to be interpreted with caution as each measurement for a full sample will be dependent on how wide a range of physical properties, such as luminosity, is covered. To properly compare samples and investigate the redshift evolution of the clustering and dark matter halo properties of galaxies, we need to then study the various dependencies between galaxies and haloes.

## 4.2 Stellar mass dependency on halo mass

An SHM relationship has been extensively observed in the literature and forms the main basis of the abundance matching technique (e.g. Vale & Ostriker 2004; Leauthaud et al. 2011, 2012; Behroozi et al. 2013b; Moster, Naab & White 2013; Coupon et al. 2015; Moster, Naab & White 2017). Since our samples are not stellar mass-complete, a comparison of the SHM relationship between our measurements and abundance matching measurements can test the accuracy of our models. Exploring trends between stellar mass and halo mass also allows us to understand how one of the fundamental properties of galaxies is related to the fundamental property of dark matter haloes with our unique sample of active, star-forming galaxies.

Fig. 5 shows the changes in $r_0$ per stellar mass bin for our samples with the results tabulated in Tables 3 and 4. We find $r_0$ increasing by a factor of ∼2 with increasing stellar mass for $z = 0.84$ H $\beta$ + [O III] emitters and a shallower increase for the $z > 1$ H $\beta$ + [O III] emitters. Similar trends for the [O II] emitters are also observed, although we can only make such statements regarding the $z < 3$ samples since the higher-$z$ [O II] samples are not sufficiently populated to subdivide them in stellar mass. We find a strong, redshift evolution in $r_0$ for fixed stellar mass for both H $\beta$ + [O III] and [O II] emitters. The results above are in agreement with the basic assumption of abundance matching that massive galaxies are more clustered than low-mass galaxies.

Fig. 6 shows the dependency between stellar and minimum halo mass for all redshift slices. We find a strong, redshift-independent trend between stellar and halo mass for both the H $\beta$ + [O III] and [O II] emitters where galaxies with higher stellar masses reside in higher mass haloes. For the H $\beta$ + [O III] sample, we notice that although the measurements are consistent with each other at a given stellar mass for all redshifts, the slope of the trend decreases such that by $z \gtrsim 2.2$, the trend is flat. Interestingly, these measurements occur in the same mass range ($9.2 < \log_{10} M_{stellar}/M_\odot < 11.0$) where for all redshifts, the trend is flat and then increases for higher stellar masses. A similar flat, redshift-independent trend is seen for [O II] emitters within the stellar mass range of $10^{9.75-11.0}$ M$_\odot$.

Fig. 7 shows the SHM ratio as a function of stellar mass, where we find it to be redshift-independent for all stellar masses. We find the SHM ratio for $z = 0.84$ and 1.42 H $\beta$ + [O III] emitters to be constant between $8.5 < \log_{10} M_{stellar}/M_\odot < 9.75$ and increasing for all redshift slices at $M_{stellar} > 10^{9.75}$ M$_\odot$. The [O II] emitters show a continuous increase in the SHM ratio from the lowest masses to the highest masses probed.

Overlaid in Fig. 7 are the measurements of Behroozi et al. (2013b), which used abundance matching along with constraints from observational measurements of global stellar mass functions to calculate the SHM ratio up to $z \sim 8$. Behroozi et al. (2013b) found that the ratio is redshift-independent and we therefore only highlight in Fig. 7 the $1\sigma$ confidence region of their measurements that correspond to the redshifts of our sample. We find that all four redshift slices for the [O II] samples are in agreement with the Behroozi et al. (2013b) measurements. Our H $\beta$ + [O III] measurements are also in agreement for $M_{stellar} < 10^{9.5}$ M$_\odot$ and $>10^{10}$ M$_\odot$. Note that the Behroozi et al. (2013b) measurements are based on 'global' (passive+active galaxy) stellar mass functions, while our samples are comprised of 'active' galaxies (see fig. 3 of Khostovan et al. (2016) for the *UVJ* diagram), which could explain the discrepancy at ∼$10^{9.75}$ M$_\odot$ shown in Fig. 7 for the H $\beta$ + [O III] samples. The results suggest that our halo mass measurements derived from
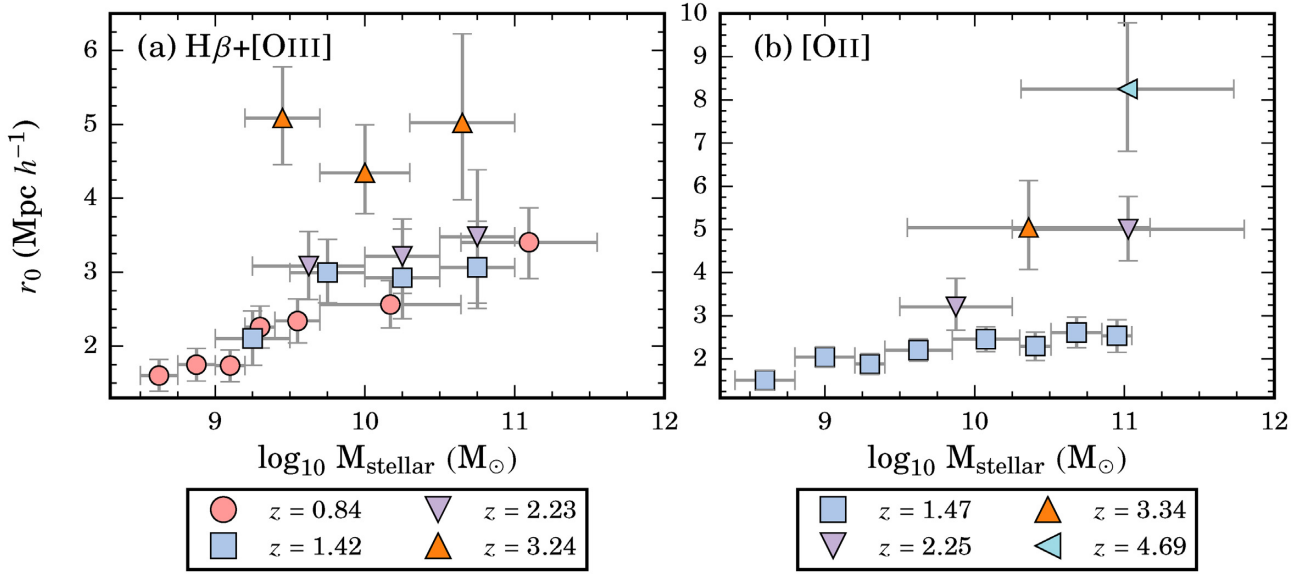
**Figure 5.** The clustering length as measured per stellar mass bins. We find that for both H $\beta$ + [O III] and [O II] emitters, the clustering length increases with increasing stellar mass. Our results show that $r_0$ also increases with redshift for a fixed stellar mass. In comparison to the line luminosity dependency, we find that the increasing trend with stellar mass is weaker, but we note that this could be a result of the line luminosity dependency or vice versa. This is because for each stellar mass bin, there is a wide range of line luminosities. We explore this interdependency in Section 4.4.

our dark matter halo models are able to reproduce the SHM ratio, although we discuss the caveats in the section below.

The comparison with Behroozi et al. (2013b) is not exactly a like-to-like comparison as their measurements are constrained using global stellar mass functions. Our samples are emission line-selected, such that they are selecting the active population of galaxies and are not stellar mass complete. Furthermore, the halo masses reported in Behroozi et al. (2013b) are defined as the mass of a host halo similar to an effective halo mass. Their models also take into account satellite galaxies, while our model assumes one central galaxy per host dark matter halo. We note that, as shown in Appendix B, our minimum halo masses are consistent with effective halo masses reported in the literature due to our halo model assumptions. Our measurements shown in Fig. 7 then have the main caveat of stellar mass incompleteness.

Despite this caveat, it is interesting that our measurements of the SHM ratio are consistent with those of Behroozi et al. (2013b). The strong agreement with our [O II] SHM ratio measurements shown in Fig. 7 also suggests that our [O II] samples are more representative of a stellar mass-complete sample in comparison to our H $\beta$ + [O III] samples. Also, the agreement provides more evidence on top of what is shown in Appendix B that the minimum halo masses measured using our halo models are consistent with effective halo masses.

### 4.3 Observed line luminosity dependency on halo mass

As discussed in Section 4.1, the clustering properties of galaxies are tied to their physical properties such that an investigation of their dependencies is required to properly map out the clustering evolution and study the connection between dark matter haloes and galaxies. In this section, we study how the clustering length and halo properties are dependent on the observed line luminosities.

Fig. 8 shows the $r_0$ dependency with line luminosity normalized by the characteristic line luminosity at the corresponding redshift,

$L/L^\star(z)$, with the tabulated measurements shown in Tables 3 and 4. We show our measurements in terms of $L/L^\star(z)$ so that we may investigate the clustering evolution of our samples independent of the cosmic evolution of the line luminosity functions. This was motivated by the results of Sobral et al. (2010) and Cochrane et al. (2017) for their H $\alpha$ samples. Khostovan et al. (2015) showed that $L^\star(z)$ can evolve by a factor of $\sim$11–12 from $z \sim 0.8$–5 for both H $\beta$ + [O III]- and [O II]-selected samples.

For each redshift slice, we find that $r_0$ strongly increases with increasing line luminosity for both H $\beta$ + [O III] and [O II] emitters. A redshift evolution is also seen at fixed $L/L^\star(z)$ for both emission line samples such that galaxies with increasing line luminosity and redshift are more clustered. Although our results suggest some redshift evolution in the clustering of galaxies as a function of line luminosity, we must also take into account the intrinsic clustering evolution due to haloes as shown in Fig. 4. A reasonable way to assess if there is an evolution in the clustering properties is by investigating it in terms of halo masses and $L/L^\star(z)$. This relation was first studied by Sobral et al. (2010) for H $\alpha$ emitters up to $z = 2.23$ where they reported a strong, redshift-independent trend between halo mass and $L/L^\star(z)$. Here we investigate if such a relation exists for our H $\beta$ + [O III] and [O II] emitters to even higher redshifts.

Fig. 9 shows the line luminosity dependence on minimum dark matter halo masses. We find that there is a strong relationship between line luminosity and halo mass for all redshift samples. More interestingly, we find no significant redshift evolution in the minimum dark matter halo mass such that galaxies reside in haloes with similar masses independent of redshift at fixed $L/L^\star(z)$. This is found for both H $\beta$ + [O III] and [O II], as well as H $\alpha$ studies (Geach et al. 2008; Shioya et al. 2008; Sobral et al. 2010; Cochrane et al. 2017) as shown in the bottom panel of Fig. 9.

We quantify the observed trends by fitting both single and piecewise power laws to all measurements at all redshifts. The piecewise power laws are used in order to test the significance of a possible flattening of the observed, increasing trends for $L > L^\star(z)$. Our

**Table 3.** Clustering properties of the H $\beta$ + [O III] samples as a function of line luminosities and stellar masses. We include $L^\star(z)$ for each sample as measured by Khostovan et al. (2015). All measurements assume a fixed $\gamma = -1.8$. The minimum dark matter halo masses are measured from the $r_0$ measurements in conjunction with our $r_0$-halo mass models. All measurements are corrected for cosmic variance by adding in quadrature 11 per cent of $r_0$ in the total error cited.

| Subsample | $N_D$ | $r_{0,\,exact}$ (Mpc $h^{-1}$) | $\log_{10} M_{min}$ (M$_\odot$ $h^{-1}$) |
|---|---|---|---|
| H $\beta$ + [O III] $z = 0.84$ ($\log_{10} L^\star = 41.79^{+0.03}_{-0.05}$) | | | |
| $40.50 < \log_{10} L_{line} < 40.60$ | 188 | $1.15^{+0.23}_{-0.22}$ | $9.48^{+1.40}_{-1.30}$ |
| $40.60 < \log_{10} L_{line} < 40.70$ | 175 | $1.46^{+0.23}_{-0.22}$ | $10.66^{+0.59}_{-0.57}$ |
| $40.70 < \log_{10} L_{line} < 40.80$ | 150 | $1.46^{+0.26}_{-0.25}$ | $10.67^{+0.67}_{-0.63}$ |
| $40.80 < \log_{10} L_{line} < 41.00$ | 279 | $1.46^{+0.20}_{-0.21}$ | $10.67^{+0.52}_{-0.52}$ |
| $41.00 < \log_{10} L_{line} < 41.15$ | 538 | $1.77^{+0.22}_{-0.21}$ | $11.28^{+0.34}_{-0.34}$ |
| $41.15 < \log_{10} L_{line} < 41.30$ | 404 | $1.89^{+0.23}_{-0.23}$ | $11.46^{+0.31}_{-0.31}$ |
| $41.30 < \log_{10} L_{line} < 41.60$ | 492 | $2.08^{+0.25}_{-0.24}$ | $11.69^{+0.28}_{-0.27}$ |
| $41.60 < \log_{10} L_{line} < 41.80$ | 131 | $3.18^{+0.44}_{-0.42}$ | $12.53^{+0.23}_{-0.22}$ |
| $41.80 < \log_{10} L_{line} < 41.95$ | 51 | $3.24^{+0.51}_{-0.46}$ | $12.55^{+0.26}_{-0.24}$ |
| $41.95 < \log_{10} L_{line} < 42.55$ | 61 | $4.64^{+0.59}_{-0.60}$ | $13.10^{+0.17}_{-0.18}$ |
| $8.50 < \log_{10} M < 8.75$ | 368 | $1.60^{+0.22}_{-0.21}$ | $11.15^{+0.32}_{-0.32}$ |
| $8.75 < \log_{10} M < 9.00$ | 483 | $1.75^{+0.22}_{-0.22}$ | $11.35^{+0.28}_{-0.28}$ |
| $9.00 < \log_{10} M < 9.20$ | 391 | $1.74^{+0.21}_{-0.22}$ | $11.33^{+0.27}_{-0.28}$ |
| $9.20 < \log_{10} M < 9.40$ | 294 | $2.26^{+0.28}_{-0.28}$ | $11.89^{+0.26}_{-0.26}$ |
| $9.40 < \log_{10} M < 9.70$ | 271 | $2.34^{+0.30}_{-0.29}$ | $11.96^{+0.26}_{-0.26}$ |
| $9.70 < \log_{10} M < 10.64$ | 213 | $2.56^{+0.32}_{-0.32}$ | $12.11^{+0.20}_{-0.19}$ |
| $10.64 < \log_{10} M < 11.55$ | 74 | $3.41^{+0.46}_{-0.49}$ | $12.55^{+0.21}_{-0.22}$ |
| H $\beta$ + [O III] $z = 1.42$ ($\log_{10} L^\star = 42.06^{+0.06}_{-0.05}$) | | | |
| $41.92 < \log_{10} L_{line} < 42.02$ | 191 | $1.54^{+0.28}_{-0.25}$ | $10.87^{+0.49}_{-0.44}$ |
| $42.02 < \log_{10} L_{line} < 42.06$ | 63 | $2.33^{+0.49}_{-0.48}$ | $11.79^{+0.40}_{-0.39}$ |
| $42.06 < \log_{10} L_{line} < 42.16$ | 58 | $4.30^{+0.67}_{-0.68}$ | $12.78^{+0.22}_{-0.22}$ |
| $42.16 < \log_{10} L_{line} < 42.26$ | 25 | $4.28^{+1.12}_{-1.08}$ | $12.78^{+0.36}_{-0.35}$ |
| $42.26 < \log_{10} L_{line} < 42.80$ | 34 | $3.97^{+0.82}_{-0.84}$ | $12.67^{+0.30}_{-0.31}$ |
| $9.00 < \log_{10} M < 9.50$ | 96 | $2.10^{+0.38}_{-0.36}$ | $11.54^{+0.33}_{-0.31}$ |
| $9.50 < \log_{10} M < 10.00$ | 99 | $3.00^{+0.45}_{-0.41}$ | $12.14^{+0.21}_{-0.19}$ |
| $10.00 < \log_{10} M < 10.50$ | 60 | $2.93^{+0.66}_{-0.55}$ | $12.11^{+0.31}_{-0.26}$ |
| $10.50 < \log_{10} M < 11.00$ | 53 | $3.06^{+0.62}_{-0.55}$ | $12.18^{+0.28}_{-0.25}$ |
| H $\beta$ + [O III] $z = 2.23$ ($\log_{10} L^\star = 42.66^{+0.13}_{-0.13}$) | | | |
| $42.30 < \log_{10} L_{line} < 42.66$ | 136 | $2.66^{+0.44}_{-0.44}$ | $11.77^{+0.28}_{-0.28}$ |
| $42.66 < \log_{10} L_{line} < 42.74$ | 56 | $5.15^{+0.64}_{-0.68}$ | $12.74^{+0.16}_{-0.17}$ |
| $42.74 < \log_{10} L_{line} < 43.10$ | 57 | $7.38^{+0.88}_{-0.90}$ | $13.17^{+0.14}_{-0.14}$ |
| $9.25 < \log_{10} M < 10.00$ | 120 | $3.08^{+0.47}_{-0.45}$ | $11.89^{+0.26}_{-0.25}$ |
| $10.00 < \log_{10} M < 10.50$ | 66 | $3.22^{+0.50}_{-0.50}$ | $11.97^{+0.27}_{-0.27}$ |
| $10.50 < \log_{10} M < 11.00$ | 41 | $3.48^{+0.91}_{-0.90}$ | $12.08^{+0.35}_{-0.34}$ |
| H $\beta$ + [O III] $z = 3.24$ ($\log_{10} L^\star = 42.83^{+0.19}_{-0.17}$) | | | |
| $42.30 < \log_{10} L_{line} < 42.67$ | 68 | $3.24^{+0.51}_{-0.53}$ | $11.77^{+0.24}_{-0.25}$ |
| $42.67 < \log_{10} L_{line} < 42.83$ | 67 | $5.56^{+0.74}_{-0.73}$ | $12.52^{+0.17}_{-0.17}$ |
| $42.83 < \log_{10} L_{line} < 43.18$ | 44 | $6.98^{+1.12}_{-1.00}$ | $12.80^{+0.19}_{-0.17}$ |
| $9.20 < \log_{10} M < 9.70$ | 56 | $5.09^{+0.69}_{-0.63}$ | $12.29^{+0.18}_{-0.17}$ |
| $9.70 < \log_{10} M < 10.30$ | 80 | $4.35^{+0.65}_{-0.55}$ | $12.08^{+0.20}_{-0.17}$ |
| $10.30 < \log_{10} M < 11.00$ | 29 | $5.02^{+1.21}_{-1.04}$ | $12.27^{+0.32}_{-0.28}$ |

**Table 4.** The clustering properties of [O II] as a function of line luminosity and stellar mass. Table description is the same as that of Table 3. The $z = 3.34$ and 4.69 measurements are not included in this table as the sample sizes were too small to divide in line luminosity and stellar mass bins. The measurements corresponding to the full samples are shown in Table 1.

| Subsample | $N_D$ | $r_{0,\,exact}$ (Mpc $h^{-1}$) | $\log_{10} M_{min}$ (M$_\odot$ $h^{-1}$) |
|---|---|---|---|
| [O II] $z = 1.47$ ($\log_{10} L^\star = 41.86^{+0.03}_{-0.03}$) | | | |
| $41.05 < \log_{10} L_{line} < 41.15$ | 200 | $1.34^{+0.27}_{-0.22}$ | $10.47^{+0.61}_{-0.51}$ |
| $41.15 < \log_{10} L_{line} < 41.25$ | 501 | $1.41^{+0.18}_{-0.18}$ | $10.62^{+0.37}_{-0.36}$ |
| $41.25 < \log_{10} L_{line} < 41.45$ | 761 | $1.74^{+0.20}_{-0.20}$ | $11.16^{+0.27}_{-0.28}$ |
| $41.45 < \log_{10} L_{line} < 41.65$ | 638 | $2.47^{+0.29}_{-0.29}$ | $11.89^{+0.21}_{-0.22}$ |
| $41.65 < \log_{10} L_{line} < 41.85$ | 667 | $2.76^{+0.32}_{-0.32}$ | $12.08^{+0.20}_{-0.20}$ |
| $41.85 < \log_{10} L_{line} < 42.00$ | 292 | $3.34^{+0.40}_{-0.40}$ | $12.39^{+0.19}_{-0.19}$ |
| $42.00 < \log_{10} L_{line} < 42.10$ | 101 | $3.23^{+0.46}_{-0.49}$ | $12.34^{+0.23}_{-0.24}$ |
| $42.10 < \log_{10} L_{line} < 42.20$ | 68 | $3.32^{+0.49}_{-0.50}$ | $12.38^{+0.23}_{-0.24}$ |
| $42.20 < \log_{10} L_{line} < 42.60$ | 56 | $4.06^{+0.88}_{-0.70}$ | $12.68^{+0.31}_{-0.25}$ |
| $8.40 < \log_{10} M < 8.80$ | 217 | $1.51^{+0.23}_{-0.23}$ | $10.84^{+0.49}_{-0.49}$ |
| $8.80 < \log_{10} M < 9.20$ | 671 | $2.04^{+0.24}_{-0.24}$ | $11.48^{+0.21}_{-0.21}$ |
| $9.20 < \log_{10} M < 9.40$ | 429 | $1.88^{+0.24}_{-0.24}$ | $11.33^{+0.24}_{-0.23}$ |
| $9.40 < \log_{10} M < 9.85$ | 840 | $2.20^{+0.26}_{-0.25}$ | $11.61^{+0.21}_{-0.21}$ |
| $9.85 < \log_{10} M < 10.30$ | 492 | $2.46^{+0.29}_{-0.29}$ | $11.81^{+0.21}_{-0.21}$ |
| $10.30 < \log_{10} M < 10.51$ | 163 | $2.30^{+0.33}_{-0.33}$ | $11.69^{+0.25}_{-0.26}$ |
| $10.51 < \log_{10} M < 10.85$ | 203 | $2.61^{+0.36}_{-0.35}$ | $11.92^{+0.25}_{-0.24}$ |
| $10.85 < \log_{10} M < 11.05$ | 97 | $2.54^{+0.37}_{-0.39}$ | $11.86^{+0.27}_{-0.28}$ |
| [O II] $z = 2.25$ ($\log_{10} L^\star = 42.34^{+0.04}_{-0.03}$) | | | |
| $42.40 < \log_{10} L_{line} < 42.57$ | 102 | $2.97^{+0.42}_{-0.42}$ | $11.95^{+0.22}_{-0.22}$ |
| $42.57 < \log_{10} L_{line} < 43.21$ | 35 | $4.49^{+0.75}_{-0.73}$ | $12.55^{+0.23}_{-0.22}$ |
| $9.50 < \log_{10} M < 10.25$ | 61 | $3.21^{+0.66}_{-0.54}$ | $11.95^{+0.36}_{-0.29}$ |
| $10.25 < \log_{10} M < 11.80$ | 43 | $5.01^{+0.76}_{-0.73}$ | $12.56^{+0.21}_{-0.20}$ |

single power-law fits are

$$\frac{M_{min}}{M_\odot/h} = \begin{cases} 10^{12.48\pm0.07}\left(\frac{L}{L^\star(z)}\right)^{1.77\pm0.21} & H\beta + [O\,III] \\ 10^{12.87\pm0.06}\left(\frac{L}{L^\star(z)}\right)^{1.17\pm0.14} & H\alpha \end{cases}, \quad (7)$$

where we only show the measurements for H $\beta$ + [O III] and H $\alpha$ as the [O II] measurements show a clear deviation for $L > L^\star(z)$. We find that the H $\beta$ + [O III] emitters show a steeper increasing trend in comparison to H $\alpha$ but with a lower halo mass at $L \sim L^\star(z)$. This could be due to a higher population of [O III]-selected AGNs that reside in massive haloes compared to H $\alpha$, which we discuss in Section 5.

Fig. 9 shows a clear deviation from a single power-law trend at $L \sim L^\star(z)$ for the [O II] samples. There is some signature of such a deviation in our H $\beta$ + [O III] and also the H $\alpha$ samples from the literature where the slope of the trends becomes shallower. We fit piecewise power laws split at $L \sim L^\star(z)$ and find

H $\beta$ + [O III]:

$$\frac{M_{min}}{M_\odot/h} = 10^{12.56\pm0.11} \begin{cases} \left(\frac{L}{L^\star(z)}\right)^{2.02\pm0.32} & L < L^\star \\ \left(\frac{L}{L^\star(z)}\right)^{1.35\pm0.47} & L > L^\star \end{cases} \quad (8)$$

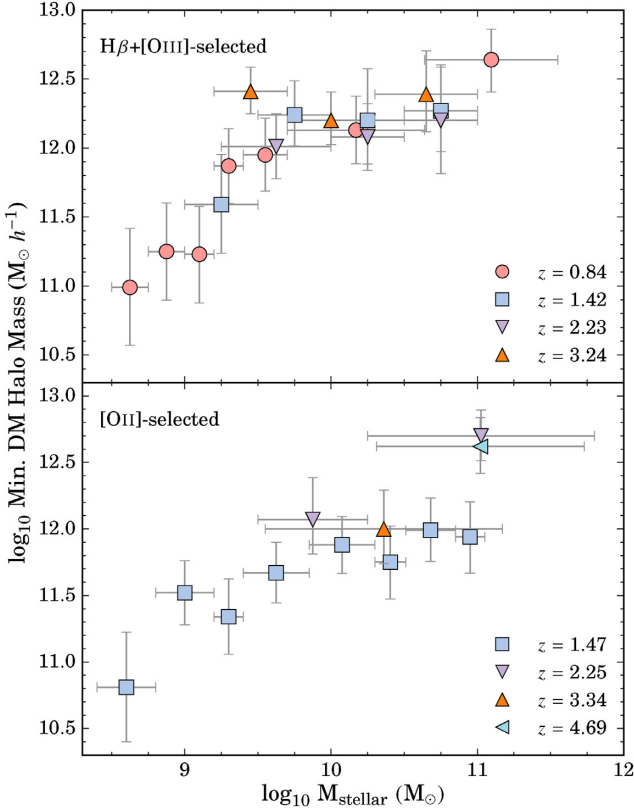**Figure 6.** The minimum halo mass dependency with stellar mass. We find a strong relationship at all redshift slices for our H $\beta$ + [O III] samples and for the $z$ = 1.47 [O II] sample. The $z$ = 2.25 [O II] sample also shows an increasing trend, but is limited only to two stellar mass bins. The other [O II] samples are limited due to sample size and could not be separated in stellar mass bins. We find no redshift evolution in the relationship. Interestingly, at stellar masses >$10^{9.75}$ M$_\odot$, the halo mass is found to be constant at ~$10^{12.3}$ M$_\odot$ for H $\beta$ + [O III] emitters and ~$10^{12}$ M$_\odot$ for [O II] emitters.

[O II]:

$$\frac{M_{min}}{M_\odot/h} = 10^{12.39\pm0.08} \begin{cases} \left(\frac{L}{L^\star(z)}\right)^{2.37\pm0.31} & L < L^\star \\ \left(\frac{L}{L^\star(z)}\right)^{0.003\pm0.003} & L > L^\star \end{cases} \quad (9)$$

H $\alpha$:

$$\frac{M_{min}}{M_\odot/h} = 10^{13.04\pm0.08} \begin{cases} \left(\frac{L}{L^\star(z)}\right)^{0.36\pm0.20} & L < 0.3L^\star \\ \left(\frac{L}{L^\star(z)}\right)^{2.61\pm0.36} & 0.3L^\star < L < L^\star \\ \left(\frac{L}{L^\star(z)}\right)^{0.87\pm0.43} & L > L^\star \end{cases} \quad (10)$$

where only the H $\alpha$ measurements include a second split at $L \sim 0.3L^\star$, which is only constrained by the $z \sim 0.24$ H $\alpha$ measurements of Shioya et al. (2008). Therefore, we cannot state that the trend is redshift-independent below $0.3L^\star$ for H $\alpha$-selected emitters due to lack of measurements at different redshifts.

Equations (8)–(10) show a steep, increasing trend up to $L \sim L^\star$ followed by significantly shallower slopes beyond $L*$. The H $\beta$ + [O III] fit shows the steepest slope of $1.35 \pm 0.47$ beyond $L^\star$, which could be due to a higher AGN fraction compared to H $\alpha$ and [O II] since the [O III] line is a high ionization potential line that can be very bright due to intense star formation and/or AGN activity. The fits confirm a near constant halo mass for $L > L^\star(z)$ such that emission line-selected galaxies (H $\alpha$, H $\beta$ + [O III], and [O II]) with
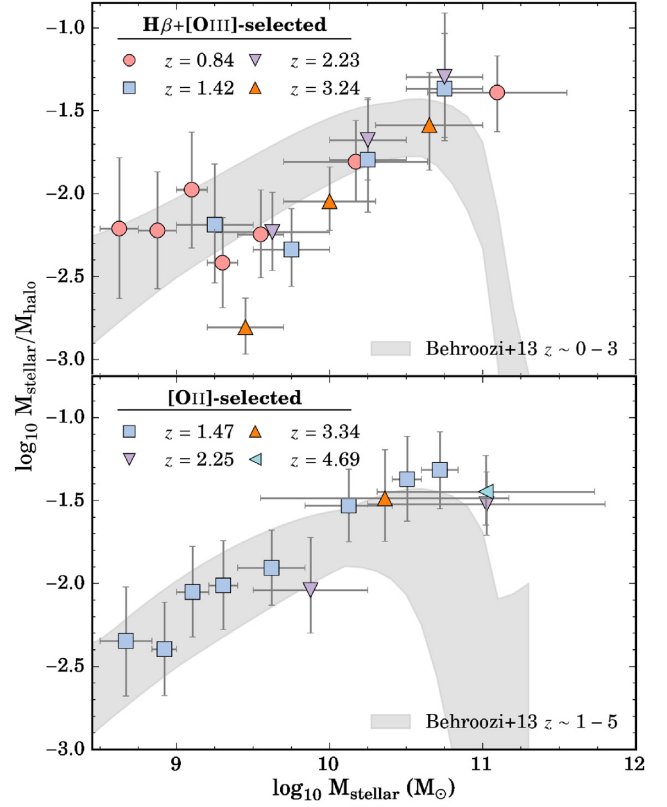


**Figure 7.** The SHM ratio as a function of stellar mass. We find our [O II] measurements show a continuous, redshift-independent increase in the SHM ratio for the full stellar mass range. The H $\beta$ + [O III] measurements show a constant ratio up to ~$10^{9.75}$ M$_\odot$ followed by a continuous, redshift-independent increase in the ratio. We compare our measurements with the abundance matching measurements of Behroozi, Wechsler & Conroy (2013b) overlaid in grey. We find that our [O II] and H $\beta$ + [O III] measurements are in agreement within $1\sigma$ except for our H $\beta$ + [O III] $10^{9.75-10.00}$ M$_\odot$ measurements.

different line luminosities >$L^\star$ reside in haloes with similar masses independent of redshift. This suggests that the mechanisms and processes causing this flattening of the line luminosity–halo mass relation is possibly the same in H $\alpha$, H $\beta$ + [O III], and [O II] emitters for all redshift slices probed. We discuss the physical causes of the shallower/flat trend in Section 5. The flat/shallower slope could also be due to the lower number density of $10^{12.5-13.0}$ M$_\odot$ haloes given the comoving volume of our survey.

Our results also imply that there is a simple, redshift-independent relationship between the emission line luminosities of galaxies and their host haloes once accounting for the evolution in $L^\star$ (Sobral et al. 2010). This has implications for theoretical studies that use photoionization codes along with semianalytical modelling to study the connection between nebular emission lines and dark matter halo properties (e.g. Orsi et al. 2014).

The results reported in equations (7)–(10) and shown in Fig. 9 do not take into account the errors in $L^\star(z)$. The errors for each sample are listed in Tables 3 and 4. We find that the errors are on the order of 0.05 dex for the lowest redshift samples and ~0.20 dex for the highest redshift samples. Taking into account this error does not significantly remove the redshift independency seen in Fig. 9, but may change the measurements shown in equations (7)–(10).
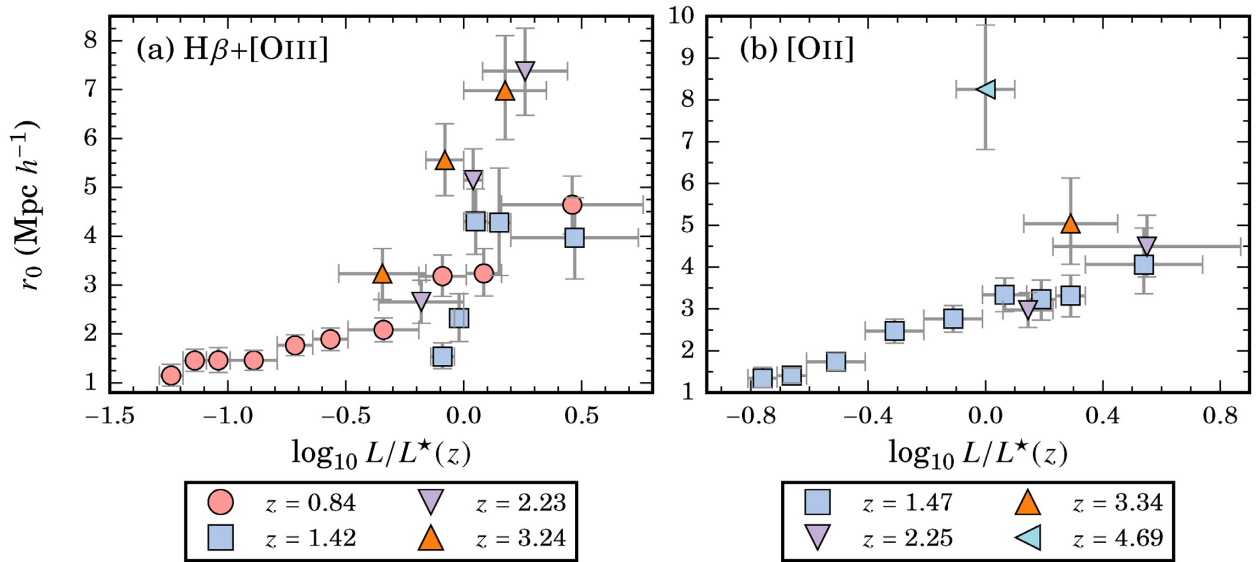
**Figure 8.** The clustering length measured in terms of $L/L^{\star}(z)$. Studying the dependency of the clustering length with luminosity as a function of the ratio between line and characteristic luminosity removes the effects caused by the cosmic evolution in the luminosity functions. For each redshift slice, we find that there is a strong correlation between the clustering length and $L/L^{\star}(z)$. There is an evolution in the clustering length such that $r_0$ increases with redshift at any given $L/L^{\star}(z)$. For example, the clustering lengths at $L \sim L^{\star}(z)$ are 3.2, 4.3, 5.2, and 7.0 $h^{-1}$ Mpc for our H $\beta$ + [O III] samples at $z = 0.84$, 1.42, 2.23, and 3.24. The same strong, increasing trend between $r_0$ and $L/L^{\star}(z)$ is also seen for the [O II] sample.

### 4.4 Observed line luminosity–stellar mass dependency on halo mass

Observations have found a correlation between the star formation rate and stellar mass in the local Universe (e.g. Salim et al. 2007; Lee et al. 2011), around cosmic noon (e.g. Daddi et al. 2007; Noeske et al. 2007; Rodighiero et al. 2011; Whitaker et al. 2014; Shivaei et al. 2015), and at higher redshifts (e.g. Schreiber et al. 2015; Tasca et al. 2015; Tomczak et al. 2016). Line luminosities trace star formation activity (e.g. [O III]: Suzuki et al. 2016; [O II]: Kennicutt 1998; Kewley, Geller & Jansen 2004) and we find a dependence between halo mass, line luminosity, and stellar mass. The question that arises is how much does the dependency of line luminosity affect the dependency measured with stellar mass or vice versa?

We test this by redoing our clustering analysis in 10 000 randomly selected parts of the line luminosity–stellar mass grid and calculate the halo mass following the same methodology highlighted in Section 3.2. Each realization is a rectangular box randomly placed in the grid and must have >50 sources. The results are shown in Fig. 10 for only the NB921 samples (H $\beta$ + [O III] $z = 0.84$ and [O II] $z = 1.47$) as these are the most populated samples and are much easier to investigate the dual dependency of line luminosity and stellar mass with the halo mass. We find that for increasing line luminosity and stellar mass, the halo mass is increasing from as low as $10^8$ to $10^{13}$ $M_{\odot}$, although there is a significant scatter such that to assess which property dominates the dependency with halo mass requires a look at how stellar mass (line luminosity) is dependent on halo mass for a fixed line luminosity (stellar mass).

We first investigate if there is a line luminosity dependency for a fixed stellar mass. We find a strong dependency between halo mass and line luminosity in H $\beta$ + [O III] emitters with fixed stellar masses of $10^{8.5-9.5}$ $M_{\odot}$, where the halo mass is found to increase from $\sim 10^{8.0}$ to $\sim 10^{12.5-13.0}$ $M_{\odot}$. Beyond >$10^{9.5}$ $M_{\odot}$, the halo mass is consistent with $10^{12.5-13}$ $M_{\odot}$ for all observed line luminosities,

although this is primarily due to a small sample size (∼300 sources, see Table 3) and a limiting range of line luminosities, especially at higher stellar masses.

For the $z = 1.47$ [O II] emitters, we find that for fixed stellar masses of $10^{8.5-11}$ $M_{\odot}$, there is a strong dependency with line luminosity such that the halo mass increases from $\sim 10^{9.5}$ to $10^{13}$ $M_{\odot}$ with increasing line luminosity. Interestingly, the dependency is found for a wider range of fixed stellar masses in comparison to the H $\beta$ + [O III] sample and this could be due to the [O II] sample selecting more higher mass galaxies with low SFRs and ionization parameters compared to H $\beta$ + [O III].

In the case of a fixed line luminosity, we find that there is only a stellar mass dependency with halo mass for H $\beta$ + [O III] emitters with $L \lesssim 10^{41.5}$ erg s$^{-1}$ and it becomes more prevalent at $L \lesssim 10^{41.0}$ erg s$^{-1}$. The stellar mass dependency in the $L_{\rm H}\beta$ + [O III] $\sim 10^{41.0-41.5}$ erg s$^{-1}$ regime is probably due to contaminants, such as high-mass AGNs, that reside in haloes of $\sim 10^{13}$ $M_{\odot}$. If we disregard this subpopulation of high mass sources, then the dependency breaks down. At $L_{\rm H}\beta$ + [O III] $\lesssim 10^{41.0}$ erg s$^{-1}$, we find the dependency is the strongest where emitters with stellar masses >$10^{8.6}$ $M_{\odot}$ reside in increasingly higher mass haloes.

Fig. 10 shows no significant stellar mass dependency for $z = 1.47$ [O II] emitters at a given line luminosity >$10^{41.6}$ erg s$^{-1}$. We only find a stellar mass dependency in the case that $L_{\rm [O II]} \lesssim 10^{41.3}$ erg s$^{-1}$ where the halo mass is between $10^{11-11.5}$ $M_{\odot}$ for $8.5 < \log_{10} M_{\rm stellar}/M_{\odot} < 9$, drops to halo masses of $10^{9.5-11}$ $M_{\odot}$ for $9 < \log_{10} M_{\rm stellar}/M_{\odot} < 9.5$, and then increases to halo mass of $10^{12}$ $M_{\odot}$ with increasing stellar mass.

We find that for both H $\beta$ + [O III] and [O II] emitters, a stellar mass dependency appears for the case of faint line luminosities as opposed to the line luminosity dependency that appears for the full stellar mass range. This could suggest that the trend between halo mass and line luminosity is more significant than with stellar mass, such that the correlations we observed in stellar mass could be a result of the halo mass correlation with line luminosity for our samples.
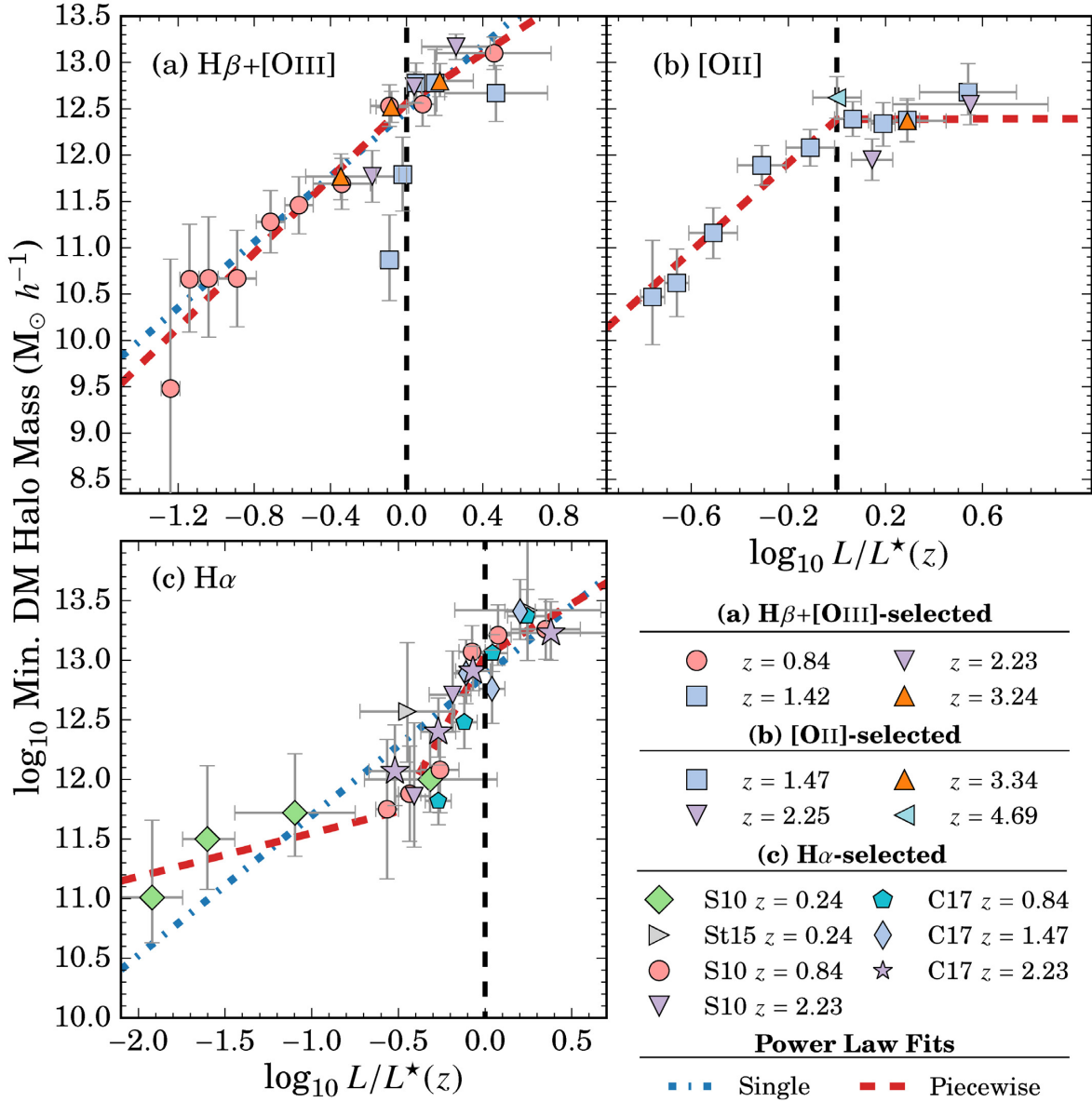
**Figure 9.** The dependency between $L/L^\star(z)$ versus minimum halo mass for our H $\beta$ + [O III] and [O II] samples. We find a strong correlation between line luminosity and dark matter halo mass and find no redshift evolution in $L/L^\star(z)$ such that galaxies at redshifts as high as $z \sim 5$ for a given $L/L^\star(z)$ reside in haloes of similar mass as galaxies at $z \sim 1$. As a comparison, we also include the H $\alpha$ measurements at $z = 0.24$ from Shioya et al. (2008) [recomputed by Sobral et al. (2010), S10)] and Stroe & Sobral (2015, St15)], $z = 0.84$ from Sobral et al. (2010), and $z = 2.23$ from Geach et al. (2008) (recomputed by Sobral et al. (2010)). The latest H $\alpha$ results of Cochrane et al. (2017, C17) are also included at $z = 0.84$, 1.47, and 2.23. The consensus from H $\alpha$ studies is a strong dependency between line luminosity and halo mass. For $L > L^\star$ emitters, we find a flat trend with halo mass consistent with $10^{12.5}$ M$_\odot$ for [O II] emitters and a shallower increasing trend for H $\alpha$ and H $\beta$ + [O III] emitters, although the scatter in the measurements is $\sim$0.5 dex, which can also be consistent with a flat trend.

Sobral et al. (2010) came to a similar conclusion using a sample of $z = 0.84$ H $\alpha$ emitters and the rest-frame $K$-band luminosity as a proxy for stellar mass. Cochrane et al. (2017) also came to a similar conclusion using samples of $z = 0.84$, 1.47, and 2.23 H $\alpha$ emitters.

## 5 DISCUSSION

In the previous sections, we found that there is a strong, redshift-independent relationship between line luminosity and minimum halo mass (relatively independent of stellar mass for $z = 0.84$ and 1.47 H $\beta$ + [O III] and [O II] emitters, respectively) up to $L \sim L^\star$ for

H $\alpha$, H $\beta$ + [O III], and [O II] emitters. For the $L > L^\star$ regime, we find that the dependency becomes shallower and is consistent with minimum halo masses between $10^{12.5}$ and $10^{13}$ M$_\odot$. In this section, we discuss potential physical reasons for the flat/shallower slope of this relationship for the brightest emitters with the understanding that the emission lines observed trace the underlying star formation activity.

### 5.1 Transitional halo mass

Current models of galaxy formation suggest that the star formation efficiency is tied to the host halo mass with a peak efficiency found in
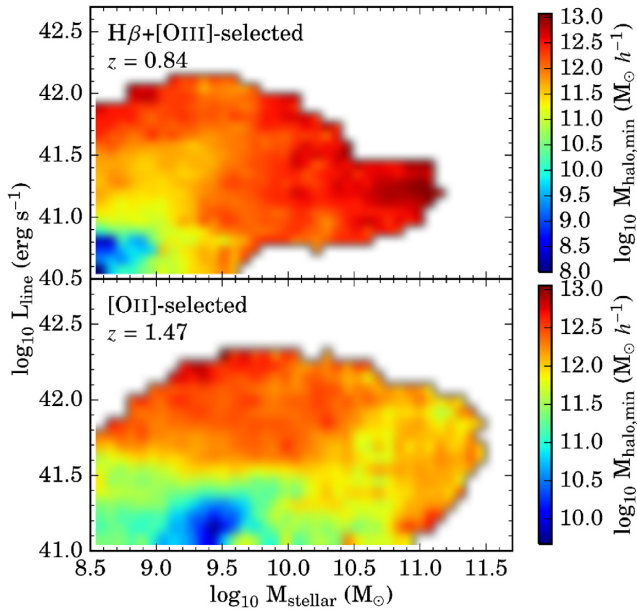
**Figure 10.** Shown is the halo mass dependency on line luminosity and stellar mass. Only the NB921 samples are used ($z = 0.84$ H $\beta$ + [O III] and $z = 1.47$ [O II]) as these are the most populated (∼2500–3000 sources each). All the measurements were done by randomly sampling the grid 10 000 times and going through the clustering analysis to measure the halo mass. Overall, we find that the halo mass correlation with line luminosity is stronger than with stellar mass.

∼$10^{12}$ M$_\odot$ haloes (e.g. Behroozi, Wechsler & Conroy 2013a). For >$10^{12}$ M$_\odot$ haloes, models predict that the star formation activity in galaxies diminishes as external quenching mechanisms (e.g. shock heating of infalling gas; Dekel & Birnboim 2006) become stronger and are accompanied by internal quenching mechanisms (e.g. AGN feedback; Best et al. 2006). This is referred to as 'halo quenching', where a specific global halo mass is related to galaxy quenching. We note that this is still debatable where, observationally, some studies have found that external quenching is mainly a local phenomenon (e.g. Darvish et al. 2016) and does not depend significantly on the global halo mass (e.g. Peng et al. 2012; Carollo et al. 2013). Other observational studies find that galaxy quenching does depend on halo mass (e.g. Prescott et al. 2011; also see references in Darvish et al. 2017).

A consequence of the halo quenching predictions is a possible transitional halo mass for which the fraction of star-forming galaxies drops and the fraction of passive galaxies increases sharply. Current predictions place this redshift-independent mass scale at a few × $10^{12}$ to $10^{13}$ M$_\odot$ (Croton et al. 2006; Dekel & Birnboim 2006; Cen 2011; Bower et al. 2017) and observations measure it at ∼5–8 × $10^{12}$ M$_\odot$ (e.g. Hartley et al. 2013; Dolley et al. 2014).

A transitional halo mass would imply that the probability of finding a star-forming galaxy above this mass scale diminishes considerably. Therefore, one would find that above a certain line luminosity, all star-forming galaxies would typically reside in haloes of a specific mass. We find such a feature in Fig. 9, where $L > L^\star$ emitters have a flat/shallower line luminosity dependency consistent with halo masses between $3 × 10^{12}$ and $10^{13}$ M$_\odot$ up to $z ∼ 5$, in agreement with predictions of a transitional halo mass.

Although we find evidence for a transitional halo mass, it raises the question of how the brightest emitters reside in $10^{13}$ M$_\odot$ haloes. Since line luminosity traces star formation activity, it then seems

puzzling that systems with such high SFRs are found in massive haloes well past the scale where peak SF efficiency occurs. One possibility is that $L > L^\star$ emitters have their emission lines powered by AGN activity. Studies of $z ∼ 0.8$–2.2 H $\alpha$ emitters find increasing AGN fractions with increasing line luminosity (Sobral et al. 2016). Typical $z ∼ 1.5$ X-ray and radio-selected AGNs are also found to reside in haloes of ∼$10^{13}$ M$_\odot$ (Hickox et al. 2009; Koutoulidis et al. 2013; Mendez et al. 2016), consistent with the constant halo mass for $L > L^\star$ H $\beta$ + [O III] and [O II] emitters. It is then quite possible that the brightest emitters in our samples are AGNs, although we require future spectroscopic confirmation.

Another possibility is that a fraction of the brightest emitters can have their emission lines powered by major merging events, such that these systems are currently undergoing a starburst phase. Simulations of major mergers predict elevated levels of star formation activity (e.g. Mihos & Hernquist 1996; Di Matteo et al. 2008; Bournaud et al. 2011) and observations have thus far found evidence to support this (e.g. Hung et al. 2013). Semianalytical models have also predicted that the stellar mass assembly in high-mass haloes is merger-driven (e.g. Zehavi, Patiri & Zheng 2012). A detailed morphological study of the fraction of mergers as a function of line luminosity would help in addressing this issue and we plan to explore this in the future.

It could also be possible that enhanced gas inflows could allow for the presence of >$L^\star$ emitters in massive haloes. Dekel & Birnboim (2006) used simulations and predict that cold filamentary streams can penetrate the shock-heated halo gas in >$3 × 10^{12}$ M$_\odot$ haloes and fuel star formation activity in $L > L^\star$ galaxies above $z > 2$. To support this level of star formation activity requires large cold gas accretion rates and a recent ALMA study by Scoville et al. (2017) estimated the rate to be >100 M$_\odot$ yr$^{-1}$ for $z > 2$ to maintain galaxies along the main sequence.

Overall, we find evidence for a possible transitional halo mass for which star-forming galaxies become less common and haloes are increasingly populated by passive galaxies. A likely possibility is that the $L > L^\star$ emitters are a mixture of AGN- and star formation-dominated systems. This is also suggested by Kauffmann et al. (2003) in the local Universe (up to $z ∼ 0.3$) where they find that galaxies with AGN and bright [O III] lines also include young stellar populations due to a recent phase of star formation activity. Future spectroscopic and morphological studies can shed light on the physical processes involved that are powering nebular emission lines in such massive haloes and provide us with valuable insight into the quenching mechanisms that are occurring at this transitional halo mass.

## 5.2 Clustering more dependent on line luminosity than stellar mass?

In Sections 4.2 and 4.4, we found that the dependency of clustering on line luminosity was more significant than on stellar mass. We also concluded, based on the results of our $z = 0.84$ H $\beta$ + [O III] and $z = 1.47$ [O II] samples in Section 4.4, the stellar mass dependency may be a result of the line luminosity dependency. This is a similar conclusion made by Sobral et al. (2010) where they used a $z = 0.84$ H $\alpha$-selected sample and found that the line luminosity dependency was more significant than the dependency with stellar mass. Coil et al. (2017) came to a similar conclusion where they found that the clustering amplitude was a stronger function of the specific SFR than stellar mass and that the clustering strength for a given specific SFR was found to be independent of stellar mass. Cochrane et al. (2017) used H $\alpha$-selected narrowband samples at $z = 0.84$, 1.47,

and 2.23 and found that the line luminosity dependency was not driven/independent of stellar mass.

We note that the lack of a strong stellar mass dependency with clustering strength/dark matter halo mass could be mainly caused by sample selection. As mentioned before, our samples are line flux-selected such that they are complete in line luminosity down to a completeness limit. Our samples are then not stellar mass complete, especially for the low stellar mass range ($<10^9$ $M_{\odot}$; see Khostovan et al. 2016 for the stellar mass functions of our samples). We can only conclude that for narrowband-selected samples, the clustering strength dependency with stellar mass seems to be less significant than the dependency with line luminosity and may also be a result of it as well.

## 6 CONCLUSIONS

We have presented our H $\beta$ + [O III] and [O II] clustering measurements up to $z \sim 3.3$ and $\sim 4.7$, respectively. The main results of this study are as follows:

(i) We find that the power-law slopes of the angular correlation functions are consistent with $\beta \sim -0.80$. Using the exact Limber equation, we find typical $r_0$ between 1.45–4.01 $h^{-1}$ Mpc and 1.99–8.25 $h^{-1}$ Mpc for H $\beta$ + [O III] and [O II] emitters, respectively. These correspond to minimum halo masses between $10^{10.70-12.08}$ and $10^{11.46-12.62}$ $M_{\odot}$, respectively.

(ii) A $r_0$-line luminosity dependency is found where the brightest emitters are more clustered compared to the faintest emitters. This dependency is found to be redshift-dependent but is biased due to the line luminosity function evolution. When rescaling based on $L^{\star}(z)$ and using model predictions of halo mass given $r_0$, we find a strong, increasing dependency between minimum halo mass and line luminosity that is independent of redshift with the faintest H $\beta$ + [O III] ([O II]) emitters found in $10^{9.5}$ $M_{\odot}$ ($10^{10.5}$ $M_{\odot}$) haloes and the brightest H $\beta$ + [O III] ([O II]) emitters in $10^{13}$ $M_{\odot}$ ($10^{12.5}$ $M_{\odot}$) haloes.

(iii) We find a redshift-independent dependency between stellar and halo mass. We find that H $\beta$ + [O III] emitters with stellar masses $>10^{9.75}$ $M_{\odot}$ reside in $10^{12.3}$ $M_{\odot}$ haloes between $z = 0.84$ and 3.24. The [O II] samples also show a dependency for the full stellar mass range.

(iv) We find that halo mass is strongly correlated with line luminosity than stellar mass when investigating the respective trends in a line luminosity–stellar mass grid space. This then suggests a simple connection between the nebular emission line properties of galaxies and their host halo mass.

(v) The line luminosity–halo mass dependency shows an increase from the faintest emitters observed to $L \sim L^{\star}(z)$. For emitters brighter than $L^{\star}$, we find that the trend is consistent with haloes between $10^{12.5-13}$ $M_{\odot}$, which is consistent with predictions of a transitional halo mass scale. The bright emitters residing in such halo masses seem to have their strong emission lines attributed to AGN activity, galaxy merging, and enhanced gas inflow.

Our results suggest a simple connection between the clustering/dark matter halo properties and nebular emission-line properties of star-forming/'active' galaxies up to $z \sim 5$. This has implications for future theoretical studies that model this connection since previous constraints were up to $z \sim 2$ for only H $\alpha$ emitters. On the observational side, future spectroscopic studies of bright, emission line-selected galaxies can allow us to investigate the dependency between the interstellar medium properties (internal mechanisms) of galaxies and massive haloes (external mechanisms). Morphological

studies of our samples can also test to see if the shape of galaxies is connected with the host halo properties. Future space-based (e.g. *JWST*, *WFIRST*, *Euclid*) and ground-based observatories (e.g. European Extremely Large Telescope, Thirty Metre Telescope) can also allow us to study the clustering properties of emission line-selected galaxies at higher redshifts and larger comoving volumes. This would allow us to see when the following redshift-independent trends that seem to have been in place since $z \sim 5$ were first established, which would present a new scaling relation for galaxy formation and evolution models. Our results also are prelude to large-scale spectroscopic surveys using the upcoming Subaru/PFS (Takada et al. 2014), VISTA/4MOST (de Jong et al. 2016), and Mayall/DESI (DESI Collaboration 2016) instruments that will observe galaxy emission lines in large comoving volumes at redshifts up to $z \sim 2.5$.

## REFERENCES

Adelberger K. L., Steidel C. C., Pettini M., Shapley A. E., Reddy N. A., Erb D. K., 2005, ApJ, 619, 697
Barone-Nugent R. L. et al., 2014, ApJ, 793, 17
Behroozi P. S., Wechsler R. H., Conroy C., 2013a, ApJ, 762, L31
Behroozi P. S., Wechsler R. H., Conroy C., 2013b, ApJ, 770, 57
Benson A. J., 2010, Phys. Rep., 495, 33
Best P. N., Kaiser C. R., Heckman T. M., Kauffmann G., 2006, MNRAS, 368, L67
Bielby R. M. et al., 2016, MNRAS, 456, 4061
Blake C., Collister A., Lahav O., 2008, MNRAS, 385, 1257
Bournaud F. et al., 2011, ApJ, 730, 4
Bower R. G., Schaye J., Frenk C. S., Theuns T., Schaller M., Crain R. A., McAlpine S., 2017, MNRAS, 465, 32
Bradshaw E. J. et al., 2013, MNRAS, 433, 194
Carollo C. M. et al., 2013, ApJ, 776, 71
Cen R., 2011, ApJ, 741, 99
Cochrane R. K., Best P. N., Sobral D., Smail I., Wake D. A., Stott J. P., Geach J. E., 2017, MNRAS, 469, 2913
Coil A. L. et al., 2008, ApJ, 672, 153
Coil A. L. et al., 2011, ApJ, 741, 8
Coil A. L., Mendez A. J., Eisenstein D. J., Moustakas J., 2017, ApJ, 838, 87
Colless M. et al., 2001, MNRAS, 328, 1039
Comparat J., Prada F., Yepes G., Klypin A., 2017, MNRAS, 469, 4157
Coupon J. et al., 2015, MNRAS, 449, 1352
Croton D. J. et al., 2006, MNRAS, 365, 11
da Cunha E., Charlot S., Elbaz D., 2008, MNRAS, 388, 1595

Daddi E. et al., 2007, ApJ, 670, 156
Darvish B., Sobral D., Mobasher B., Scoville N. Z., Best P., Sales L. V., Smail I., 2014, ApJ, 796, 51
Darvish B., Mobasher B., Sobral D., Rettura A., Scoville N., Faisst A., Capak P., 2016, ApJ, 825, 113
Darvish B., Mobasher B., Martin D. C., Sobral D., Scoville N., Stroe A., Hemmati S., Kartaltepe J., 2017, ApJ, 837, 16
Davis M. et al., 2003, in Guhathakurta P., ed., Proc. SPIE Vol. 4834, Discoveries and Research Prospects from 6- to 10-Metre-Class Telescopes II, SPIE, Bellingham, p. 161
Dawson K. S. et al., 2013, AJ, 145, 10
Dawson K. S. et al., 2016, AJ, 151, 44
de Jong R. S. et al., 2016, in Evans C. J., Simard L., Takami H., eds, Proc. SPIE Vol. 9908, Ground-based and Airborne Instrumentation for Astronomy VI, SPIE, Bellingham, p. 99081O
Dekel A., Birnboim Y., 2006, MNRAS, 368, 2
DESI Collaboration, 2016, preprint (arXiv:1611.00036)
Despali G., Giocoli C., Angulo R. E., Tormen G., Sheth R. K., Baso G., Moscardini L., 2016, MNRAS, 456, 2486
Di Matteo P., Bournaud F., Martig M., Combes F., Melchior A.-L., Semelin B., 2008, A&A, 492, 31
Diemer B., Kravtsov A. V., 2015, ApJ, 799, 108
Dolley T. et al., 2014, ApJ, 797, 125
Driver S. P. et al., 2011, MNRAS, 413, 971
Durkalec A. et al., 2015, A&A, 583, A128
Durkalec A. et al., 2018, A&A, 612, A42
Eisenstein D. J., Hu W., 1998, ApJ, 496, 605
Favole G., Rodríguez-Torres S. A., Comparat J., Prada F., Guo H., Klypin A., Montero-Dorta A. D., 2017, MNRAS, 472, 550
Garilli B. et al., 2014, A&A, 562, A23
Geach J. E., Smail I., Best P. N., Kurk J., Casali M., Ivison R. J., Coppin K., 2008, MNRAS, 388, 1473
Geach J. E., Sobral D., Hickox R. C., Wake D. A., Smail I., Best P. N., Baugh C. M., Stott J. P., 2012, MNRAS, 426, 679
Guaita L. et al., 2010, ApJ, 714, 255
Guo H. et al., 2013, ApJ, 767, 122
Guo H. et al., 2014, MNRAS, 441, 2398
Harikane Y. et al., 2016, ApJ, 821, 123
Hartley W. G. et al., 2008, MNRAS, 391, 1301
Hartley W. G. et al., 2013, MNRAS, 431, 3045
Hayashi M., Shimasaku K., Motohara K., Yoshida M., Okamura S., Kashikawa N., 2007, ApJ, 660, 72
Hickox R. C. et al., 2009, ApJ, 696, 891
Hildebrandt H. et al., 2005, A&A, 441, 905
Hung C.-L. et al., 2013, ApJ, 778, 129
Ishikawa S., Kashikawa N., Toshikawa J., Onoue M., 2015, MNRAS, 454, 205
Jose C., Lacey C. G., Baugh C. M., 2016, MNRAS, 463, 270
Kashino D. et al., 2017, ApJ, 843, 28
Kauffmann G. et al., 2003, MNRAS, 346, 1055
Kennicutt R. C., Jr, 1998, ARA&A, 36, 189
Kerscher M., Szapudi I., Szalay A. S., 2000, ApJ, 535, L13
Kewley L. J., Geller M. J., Jansen R. A., 2004, AJ, 127, 2002
Khostovan A. A., Sobral D., Mobasher B., Best P. N., Smail I., Stott J. P., Hemmati S., Nayyeri H., 2015, MNRAS, 452, 3948
Khostovan A. A., Sobral D., Mobasher B., Smail I., Darvish B., Nayyeri H., Hemmati S., Stott J. P., 2016, MNRAS, 463, 2363
Koutoulidis L., Plionis M., Georgantopoulos I., Fanidakis N., 2013, MNRAS, 428, 1382
Kravtsov A. V., Berlind A. A., Wechsler R. H., Klypin A. A., Gottlöber S., Allgood B., Primack J. R., 2004, ApJ, 609, 35
Landy S. D., Szalay A. S., 1993, ApJ, 412, 64
Lawrence A. et al., 2007, MNRAS, 379, 1599
Le Fèvre O. et al., 2005, A&A, 439, 845
Leauthaud A., Tinker J., Behroozi P. S., Busha M. T., Wechsler R. H., 2011, ApJ, 738, 45
Leauthaud A. et al., 2012, ApJ, 744, 159
Lee J. C. et al., 2011, ApJS, 192, 6

Lee K.-S., Giavalisco M., Gnedin O. Y., Somerville R. S., Ferguson H. C., Dickinson M., Ouchi M., 2006, ApJ, 642, 63
Limber D. N., 1953, ApJ, 117, 134
Lin L. et al., 2012, ApJ, 756, 71
Marulli F. et al., 2013, A&A, 557, A17
Matarrese S., Coles P., Lucchin F., Moscardini L., 1997, MNRAS, 286, 115
Matthee J., Sobral D., Oteo I., Best P., Smail I., Röttgering H., Paulino-Afonso A., 2016, MNRAS, 458, 449
McCracken H. J. et al., 2010, ApJ, 708, 202
McCracken H. J. et al., 2015, MNRAS, 449, 901
McLure R. J. et al., 2013, MNRAS, 428, 1088
Mendez A. J. et al., 2016, ApJ, 821, 55
Meneux B. et al., 2008, A&A, 478, 299
Meneux B. et al., 2009, A&A, 505, 463
Mihos J. C., Hernquist L., 1996, ApJ, 464, 641
Mo H. J., White S. D. M., 1996, MNRAS, 282, 347
Moscardini L., Coles P., Lucchin F., Matarrese S., 1998, MNRAS, 299, 95
Mostek N., Coil A. L., Cooper M., Davis M., Newman J. A., Weiner B. J., 2013, ApJ, 767, 89
Moster B. P., Naab T., White S. D. M., 2013, MNRAS, 428, 3121
Moster B. P., Naab T., White S. D. M., 2018, MNRAS, 477, 1822
Noeske K. G. et al., 2007, ApJ, 660, L43
Norberg P. et al., 2002, MNRAS, 332, 827
Norberg P., Baugh C. M., Gaztañaga E., Croton D. J., 2009, MNRAS, 396, 19
Orsi Á., Padilla N., Groves B., Cora S., Tecce T., Gargiulo I., Ruiz A., 2014, MNRAS, 443, 799
Oteo I., Sobral D., Ivison R. J., Smail I., Best P. N., Cepa J., Pérez-García A. M., 2015, MNRAS, 452, 2018
Ouchi M. et al., 2005, ApJ, 635, L117
Ouchi M. et al., 2010, ApJ, 723, 869
Ouchi M. et al., 2018, PASJ, 70, S13
Peng Y.-j., Lilly S. J., Renzini A., Carollo M., 2012, ApJ, 757, 4
Prescott M. et al., 2011, MNRAS, 417, 1374
Press W. H., Schechter P., 1974, ApJ, 187, 425
Roche N. D., Almaini O., Dunlop J., Ivison R. J., Willott C. J., 2002, MNRAS, 337, 1282
Rodighiero G. et al., 2011, ApJ, 739, L40
Salim S. et al., 2007, ApJS, 173, 267
Schreiber C. et al., 2015, A&A, 575, A74
Scoville N. et al., 2007, ApJS, 172, 1
Scoville N. et al., 2017, ApJ, 837, 150
Sheth R. K., Mo H. J., Tormen G., 2001, MNRAS, 323, 1
Shioya Y. et al., 2008, ApJS, 175, 128
Shivaei I. et al., 2015, ApJ, 815, 98
Simon P., 2007, A&A, 473, 711
Sobral D. et al., 2009, MNRAS, 398, 75
Sobral D., Best P. N., Geach J. E., Smail I., Cirasuolo M., Garn T., Dalton G. B., Kurk J., 2010, MNRAS, 404, 1551
Sobral D., Best P. N., Smail I., Geach J. E., Cirasuolo M., Garn T., Dalton G. B., 2011, MNRAS, 411, 675
Sobral D., Best P. N., Matsuda Y., Smail I., Geach J. E., Cirasuolo M., 2012, MNRAS, 420, 1926
Sobral D., Smail I., Best P. N., Geach J. E., Matsuda Y., Stott J. P., Cirasuolo M., Kurk J., 2013, MNRAS, 428, 1128
Sobral D., Best P. N., Smail I., Mobasher B., Stott J., Nisbet D., 2014, MNRAS, 437, 3516
Sobral D., Kohn S. A., Best P. N., Smail I., Harrison C. M., Stott J., Calhau J., Matthee J., 2016, MNRAS, 457, 1739
Sobral D. et al., 2017, MNRAS, 466, 1242
Stott J. P. et al., 2013, MNRAS, 436, 1130
Stroe A., Sobral D., 2015, MNRAS, 453, 242
Suzuki T. L. et al., 2016, MNRAS, 462, 181
Takada M. et al., 2014, PASJ, 66, R1
Takahashi M. I. et al., 2007, ApJS, 172, 456
Tasca L. A. M. et al., 2015, A&A, 581, A54
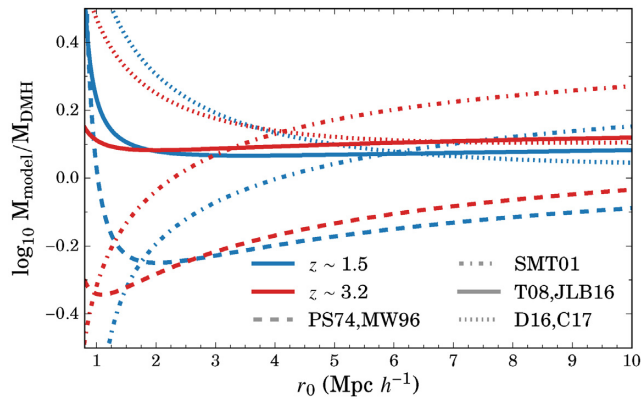Tinker J., Kravtsov A. V., Klypin A., Abazajian K., Warren M., Yepes G., Gottlöber S., Holz D. E., 2008, ApJ, 688, 709

**Figure A1.** Comparison of the predicted minimum halo masses for a given $r_0$ between our assumed halo bias (Tinker et al. 2010) and mass (Tinker et al. 2008) functions against other assumptions. The cases are as follows (mass function, bias function): (1) Press & Schechter (1974) and Mo & White (1996), (2) Sheth et al. (2001), (3) Tinker et al. (2008) and Jose et al. (2016), and (4) Despali et al. (2016) and Comparat et al. (2017). We show the difference for $z \sim 1.5$ and $\sim 3.2$ with $M_{model}/M_{DMH}$ being the ratio of one of the cases highlighted above ($M_{model}$) and our model ($M_{DMH}$). We find that assuming different prescriptions for halo properties can introduce offsets of $\sim \pm 0.2$ dex for $r_0 > 3\,\mathrm{Mpc}\,h^{-1}$ and $\pm 0.4$ dex by $r_0 \sim 1\,\mathrm{Mpc}\,h^{-1}$.

Tinker J. L., Robertson B. E., Kravtsov A. V., Klypin A., Warren M. S., Yepes G., Gottlöber S., 2010, ApJ, 724, 878
Tomczak A. R. et al., 2016, ApJ, 817, 118
Vale A., Ostriker J. P., 2004, MNRAS, 353, 189
Wake D. A. et al., 2011, ApJ, 728, 46
Whitaker K. E. et al., 2014, ApJ, 795, 104
York D. G. et al., 2000, AJ, 120, 1579
Zehavi I. et al., 2005, ApJ, 630, 1
Zehavi I. et al., 2011, ApJ, 736, 59
Zehavi I., Patiri S., Zheng Z., 2012, ApJ, 746, 145
Zheng Z. et al., 2005, ApJ, 633, 791

## APPENDIX A: EFFECTS OF HALO MODEL ASSUMPTIONS

Various prescriptions of the halo bias and mass functions exist in the literature. In this section, we explore the effects of assuming a Tinker et al. (2010) halo bias function and Tinker et al. (2008) halo mass function as opposed to other prescriptions. We consider four cases with the following mass and bias functions, respectively: (1) Press & Schechter (1974) + Mo & White (1996), (2) Sheth, Mo & Tormen (2001) for both, (3) Tinker et al. (2008) + Jose, Lacey & Baugh (2016), and (4) Despali et al. (2016) + Comparat et al. (2017).

Fig. A1 shows a comparison between our predictions of halo mass ($M_{DMH}$) and the predictions from the four cases highlighted above ($M_{model}$) for a given $r_0$ measurement at $z \sim 1.5$ and $\sim 3.2$. We find the offsets are $\sim \pm 0.2$ dex for $r_0 > 3\,\mathrm{Mpc}\,h^{-1}$ and increase to $\pm 0.4$ dex for lower clustering lengths. The third case best matches our predictions, which is not surprising as it uses the Tinker et al. (2008) halo mass function (same as the one we assumed) and the Jose et al. (2016) bias function, which is an update of the Tinker et al. (2010) bias function. Based on Fig. A1, we caution the reader that halo mass measurements, be it from our model or any HOD/abundance matching model, can be sensitive to the assumed halo prescriptions.
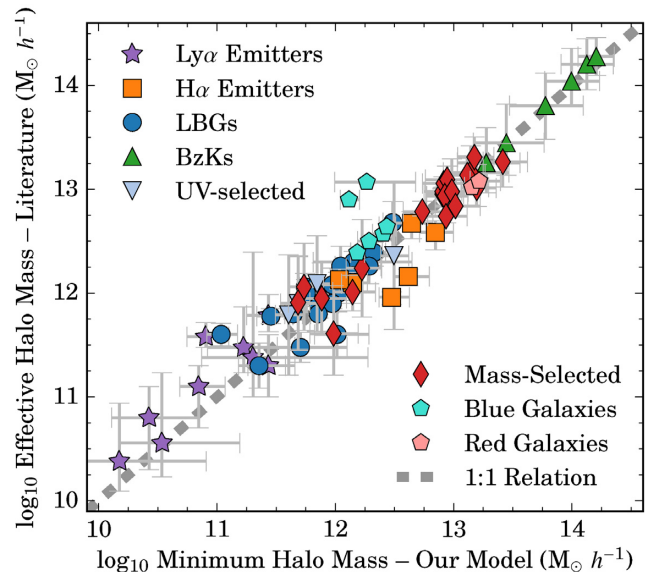
**Figure B1.** A comparison between the effective halo mass, $M_{eff}$, drawn from the literature and the minimum halo mass, $M_{min}$, measured using the clustering lengths from the literature in conjunction with our $r_0$-$M_{min}$ halo model as described in Section 3.5. We find that our simplified model (one-to-one galaxy–halo occupation) produces $M_{min}$ that is consistent with $M_{eff}$ when compared to studies using complex prescriptions for HOD models.

## APPENDIX B: MINIMUM OR EFFECTIVE HALO MASS?

We presented our dark matter halo model in Section 3.5 where we use the effective bias using a one-to-one galaxy–HOD above a minimum halo mass to connect halo mass with $r_0$ (our observable). This is a simplified approach of measuring halo mass in comparison to typical clustering/dark matter halo studies. Assuming a one-to-one galaxy–HOD is not entirely correct, especially for emission line-selected galaxies that form a subset of the total star-forming galaxy population, which forms also a subset of the global population of galaxies. We refer the reader to Cochrane et al. (2017) and Favole et al. (2017) for discussions regarding HODs of H $\alpha$ and [O II] emitters, respectively.

Comparing the stellar mass densities of the global and emission line-selected galaxies from Khostovan et al. (2016) can give us a general idea of what percentage haloes are populated by our samples. We find that H $\beta$ + [O III] emitters reside in $\sim 40$, 65, 35, and 35 per cent of haloes at $z = 0.84$, 1.42, 2.23, and 3.24, respectively. [O II] emitters are found to reside in $\sim 70$, 35, and 15 per cent of haloes at $z = 1.47$, 2.25, and 3.34 (there was no $z = 4.69$ stellar mass density measurement in Khostovan et al. (2016) due to the small sample size).

It is clear then that our emission line galaxies will not reside in every halo, such that our 'minimum' halo masses will be systematically higher. To understand what halo mass is actually being measured using our approach, we compare the predictions from our model with the literature in Fig. B1 by using $r_0$ reported in the literature and apply our model to measure $M_{min}$. Fig. B1 shows that our measurements of $M_{min}$ are strongly consistent with the effective halo mass reported in studies of Ly $\alpha$ emitters (Ouchi et al. 2010, 2018; Bielby et al. 2016), H $\alpha$ emitters (Geach et al. 2012; Cochrane et al. 2017; Kashino et al. 2017), LBGs (Hildebrandt et al. 2005; Ouchi et al. 2005; Lee et al. 2006), BzKs (Hayashi et al. 2007), UV continuum-selected (Durkalec et al. 2018), mass-selected (Wake
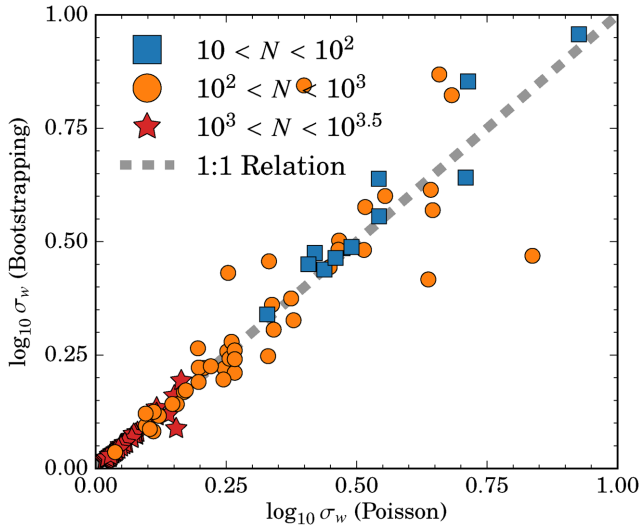
**Figure C1.** Error measurement comparison between Poisson and Bootstrapping errors. The Poisson errors measured are for single realization as described in Section 3.2. The bootstrapped errors are based on resampling a single realization of $w(\theta)$ 2000 times. For both assessments, the bin size and centres were the same in order to ensure a direct comparison. We find that for different sample sizes, $N$, the errors between Poisson and Bootstrapping are consistent.

et al. 2011; Durkalec et al. 2015, 2018), Blue galaxies (Mostek et al. 2013), and Red galaxies (Blake, Collister & Lahav 2008; Mostek et al. 2013).

The strong agreement over different sample types and redshifts ranging between local and $z \sim 7$ suggests that, due to our one-to-one galaxy–halo occupation assumption, our model predictions for halo mass are consistent with being effective halo masses rather than minimum halo masses. With this caveat, we still report our halo masses as 'minimum' as defined by our model, but note that due to our assumption regarding the occupation distribution, they better represent the effective halo mass.

## APPENDIX C: BOOTSTRAPPING AND POISSON ERRORS

There are three main error estimators that are typically employed in clustering studies: bootstrapping, jackknifing, and Poisson. In the case that Poisson errors are assumed, then the errors are defined as shown in equation (2). Norberg et al. (2009) studied these three estimators to see how reliably each measures the 'true' errors of the ACFs. They found that bootstrapping overestimates the errors by ~40 per cent and jackknifing fails at small scales but can reproduce the errors at large scales, while Poisson errors were found to underestimate the errors.

We note that the results of Norberg et al. (2009) are based on simulations that have sample sizes comparable to SDSS ($10^{5–6}$ sources) such that the Poisson errors, which are proportional to sample sizes, would severely underestimate the 'true' errors. This may not be true for our samples, which typically consist of $10^{2–3}$ sources. To test this, we measure the ACF for all the full samples with a fixed bin size and centre assuming (1) Poisson errors and (2) resampling the ACF 2000 times to measure the errors via bootstrapping.

Fig. C1 shows the comparison between the assumption of Poisson errors and bootstrapping for all our full samples. We find that our measurements assuming Poisson errors are strongly consistent with bootstrapping up to sample sizes of $10^3$. Note that we assume Poisson errors for each individual ACF but also take into account binning effects by repeating our measurements of the ACF with varying bin sizes and centres such that our final measurements are based on the distributions of these realizations.

This paper has been typeset from a TEX/LATEX file prepared by the author.